Giant hardening response in AlMgZn(Cu) alloys

Lukas Stemper [a],*, Matheus A. Tunes [b], Phillip Dumitraschkewitz [b],
Francisca Mendez-Martin [c], Ramona Tosone [d], Daniel Marchand [e], William A. Curtin [e],
Peter J. Uggowitzer [b], Stefan Pogatscher [a],*

[a] Christian Doppler Laboratory for Advanced Aluminum Alloys, Chair of Nonferrous Metallurgy, Montanuniversitaet Leoben, Franz-Josef Straße 18, 8700 Leoben, Austria
[b] Chair of Nonferrous Metallurgy, Montanuniversitaet Leoben, Franz-Josef Straße 18, 8700 Leoben, Austria
[c] Department of Materials Science, Montanuniversitaet Leoben, Franz-Josef Straße 18, 8700 Leoben, Austria
[d] AMAG rolling GmbH, Lamprechtshausener Straße 61, 5282 Ranshofen, Austria
[e] Institute of Mechanical Engineering, EPFL Lausanne, ME D3 1726, Station 9, 1015 Lausanne, Switzerland

ARTICLE INFO

ABSTRACT

This study presents a thermomechanical processing concept which is capable of exploiting the full industrial application potential of recently introduced AlMgZn(Cu) alloys. The beneficial linkage of alloy design and processing allows not only to satisfy the long-standing trade-off between high mechanical strength in use and good formability during processing but also addresses the need for economically feasible processing times. After an only 3-hour short pre-aging treatment at 100°C, the two investigated alloys, based on commercial EN AW-5182 and modified with additions of Zn and Zn+Cu respectively, show high formability due to increased work-hardening. Then, these alloys exhibit a giant hardening response of up to 184 MPa to reach a yield strength of 410 MPa after a 20-minute short final heat treatment at 185°C, i.e. paint-baking. This rapid hardening response strongly depends on the number density, size distribution and constitution of precursors acting as preferential nucleation sites for T-phase precursor precipitation during the final high-temperature aging treatment and is significantly increased by the addition of Cu. Minor deformation (2%) after pre-aging and before final heat treatment further enhances the development of hardening precipitates additionally by activating dislocation-supported nucleation and growth. Tensile testing, quantitative and analytical electron-microscopy methods, atom probe analysis and DFT calculations were used to characterize the alloys investigated in this work over the thermomechanical processing route. The influence of pre-strain on the hardening response and the role of Cu additions in early-stage cluster nucleation are discussed in detail and supported by in-situ STEM experiments and first-principles calculations.

© 2021 Acta Materialia Inc. Published by Elsevier Ltd.
This is an open access article under the CC BY-NC-ND license
(http://creativecommons.org/licenses/by-nc-nd/4.0/)

1. Introduction

Over the last decades rising CO_2 emissions associated with increasing traffic and transportation have driven the development of enhanced light-weight aluminum alloys for automotive application [1,2]. A major challenge facing these materials is the trade-off between formability and strength [3]. To overcome this trade-off, several different types of aluminum alloys are currently in-use in modern cars to fulfill the various engineering criteria, but therefore limit the recyclability at the end of a product's lifetime [4–6].

Focusing on wrought alloys, AlMgSi alloys (6xxx) are currently the dominating aluminum-based material (~60%) due to their excellent age hardening potential even though they offer only limited formability [4]. Paint-baking or bake hardening (20 min at 185°C) is the final heat treatment after forming commonly applied to car body panels to simultaneously dry the paint coating and harden the alloy by precipitation of β-phase and its precursors to adjust the in-service mechanical properties [7]. Due to the very limited variability of this process, a sufficient strength gain during this treatment - the paint bake response - is a required

* Corresponding author: Christian Doppler Laboratory for Advanced Aluminum Alloys, Chair of Nonferrous Metallurgy, Montanuniversitaet Leoben, Franz-Josef Straße 18, 8700 Leoben, Austria.

E-mail addresses: lukas.stemper@unileoben.ac.at (L. Stemper), stefan.pogatscher@unileoben.ac.at (S. Pogatscher).

attribute of aluminum alloys for industrial application in car body parts [7].

Several attempts have been made to enhance the bake hardening response of AlMgSi alloys (6xxx-series) by adapting alloy composition to reach higher total strength levels. Within standardized alloying limits, the EN AW-6016 alloy was reported to exhibit a paint bake response of 105 MPa [8] which could be significantly extended to 135 MPa with additions of Zn and Cu [9,10], thus reaching a total yield strength of 277 MPa. Although the hardening response is impressive, the final strength is still only moderate and is accompanied by reduced formability as compared to alloys within standard composition range.

In contrast to AlMgSi alloys, AlMg alloys (5xxx-series) with low strength are well established for use in components subjected to heavy deformation during processing due to their high uniform elongation and strain hardenability [4,11]. Although artificial aging is thermodynamically possible, detrimental aging kinetics and the adverse electrochemical potential of Al_3Mg_2 precipitates limit its applicability and establish solute solution hardening as the dominant strengthening mechanism in low-strength AlMg alloys [11,12]. Additionally, surface deterioration by serrated flow caused by the PLC effect [13,14] and undesired strength drop during both room temperature storage or paint bake treatment (approximately 30 MPa if 2% deformation is applied) [15,16] are limiting factors for an extended application of these alloys.

Several attempts have been made to overcome the aforementioned challenges, either to improve formability of 6xxx alloys without loss of strength [17–19] or to increase strength of 5xxx-series alloys without loss of formability. As the latter direction is the core of this present work, we now focus on the recent progress on the AlMg-based system.

Enabling precipitation hardening in 5xxx-series by adding additional alloying elements is the most common approach among recent attempts to enhance their strength. Similar to other age hardenable alloys, precipitates formed during artificial aging can act as additional obstacles to dislocation movement, resulting in increased strength [11,20].

Addition of Cu (up to 0.5 wt.%) to commercial AlMg alloys has been shown to reduce [21] or even compensate [22,23] for softening by recovery during paint bake treatment. This has been attributed to the strengthening effect of S-phase (Al_2MgCu) and its precursors [24–27].

Adding Zn (up to 3.0 wt.%) has been reported to establish precipitation of the T-$Mg_{32}(Al,Zn)_{49}$ and its precursors [28,29], resulting in increased strength [30–35], delayed onset of serrated flow [34,36–38], and enhanced corrosion resistance [30,39–41]. It is generally accepted that under equilibrium conditions, the T-phase (denoted as $Mg_3Zn_3Al_2$, $Mg_{32}(Al,Zn)_{49}$ or $Mg_{32}Zn_{31.9}Al_{17.1}$) exhibits a body-centered cubic crystal structure containing 162 atoms in its unit cell [29,42] and it can be identified according to its distinct reflection spots within the aluminum matrix along the ⟨001⟩ zone axis, exposing the characteristic T-phase spots at the 2/5 and 3/5 ⟨022⟩ Al positions [43]. The corresponding precipitation sequence, which is a key aspect in optimizing thermal treatment strategies, is still a topic of ongoing debate and research as it seems to be strongly dependent on exact alloy composition [28,29,44–47] resulting in a variety of possible precipitation sequences proposed for the Al-Mg-Zn system: *SSSS (supersaturated solid solution)* ➜ *GP (Guinier-Preston) zone* ➜ *intermediate η'* ➜ *equilibrium η* ➜ *equilibrium T* [45], *SSSS* ➜ *solute-vacancy-complex* ➜ *GP zone* ➜ *intermediate η' or T'* ➜ *equilibrium η or T* [44] and *SSSS* ➜ *GP zone* ➜ *intermediate η' or T'* ➜ *equilibrium η or T* [47].

The combined addition of Zn and Cu in AlMg alloys has recently gained increased attention due to the significant hardening response observed during the artificial aging. Investigations by transmission electron microscopy (TEM) and atom probe tomography (APT) revealed that the precipitation sequence of the hardening phases is strongly dependent on the thermal treatment routes. While peak hardness during single-step artificial aging results from the synergistic effects of T- and S-phase and/or their precursors, it is attributed to Cu-incorporated T-phase if a low-temperature pre-aging is applied before the final high-temperature aging stage [34,43,48–50]. For AlMgZn alloys with high Mg/Zn ratio and minor Cu-addition (0.15 wt.%), the evolution of precipitates has been recently proposed by Hou et al. [49] to evolve as *SSSS* ➜ *GPI-zone (fully coherent)* ➜ *GPII-zone (T'', fully coherent)* ➜ *intermediate T' (semi-coherent)* ➜ *equilibrium T (incoherent)*. It is worth emphasizing that reflection spots corresponding to T-phase were found at each development stage except for the earliest one (GPI-zone) and that neither intermediate η' nor equilibrium η was observed. The transformation was found to take place in a gradual manner, which is consistent with findings by Bigot et al. [28] reporting similar crystal structure but differing chemical compositions in intermediate T' and equilibrium T. The rate of progress of this sequence (generally associated with the hardening response) is further reported to be strongly depend on temperature and availability of Mg and Zn [49,51].

The beneficial role of Cu additions on the hardening of such alloys is well documented [34,35,50,52] and was attributed to three major aspects: (i) a stimulation of low-temperature GP-zones, which may act as preferred nuclei for T-phase precipitates in the final high-temperature ageing stage, (ii) a higher hardenability of the Cu-incorporated T-phase, and (iii) a decrease in the width of precipitation-free zones (PFZ) but the mechanisms behind these effects are still not fully understood.

In addition to alloy modification, applying a pre-deformation is also reported to have beneficial effects in various Al-alloys and has been shown to be strongly related to dislocations introduced by straining. Although the majority of published work has selected pre-deformation as a strategy to suppress natural aging by vacancy annihilation in AlMgSi alloys, a boosting effect on the artificial hardening response is also reported [7,53–55]. It seems reasonable to assume that pre-deformation might be also beneficial for the alloy system investigated here, but no information is available so far. Since these alloys are intended for application in automotive sheets, the impact of deformation-induced dislocations on the paint bake response is a crucial factor for industrial application and needs to be thoroughly assessed.

Even though some of the new AlMgZn(Cu) alloys reveal a final yield strength of over 400 MPa in peak-aged condition, the total aging time to reach such values (24h pre-aging + 25h final aging = 49h) limits their applicability in mass-production of most automotive components [49]. Previous work on the hardness evolution on similar alloys by some of the present authors shows that the hardening response observed by Hou et al. [49] can be also attained in significantly shorter aging time (3h pre-aging + 9h final aging = 12h) if alloy composition and heat treatment parameters are optimized [34] but industrial requirements have still not been met. The hardening response during short-term final heat treatments, which is the crucial factor for industrial paint baking (as mentioned before; e.g. 20 min at 185°C), was found to be only minor and has not been addressed adequately yet, with the major focus of in-depth investigations on long-term strategies [48–50]. Additionally, the evolution of mechanical behavior from the soft forming condition to the hard in-use temper is also lacking.

In this study, we propose a thermomechanical processing concept especially tailored for recently introduced AlMgZn alloys [34], focusing on one alloy with and one alloy without addition of Cu. It involves a short-term pre-aging treatment as well as a pre-straining step and is capable of meeting the main industrial processing requirements and exploiting the alloys full potential in automotive sheet production. We demonstrate a beneficial

Table 1
Measured chemical composition of the investigated alloys.

		Mg	Mn	Zn	Cu	Si	Fe	Cr
EN AW-5182	[wt.%]	4.7	0.4	-	-	0.1	0.2	0.1
	[at.%[	5.2	0.2	-	-	0.1	0.1	0.05
5182-Zn	[wt.%]	4.7	0.4	3.6	-	0.1	0.2	0.1
	[at.%[	5.3	0.2	1.5	-	0.1	0.1	0.05
5182-ZnCu	[wt.%]	4.7	0.4	3.6	0.6	0.1	0.2	0.1
	[at.%[	5.3	0.2	1.5	0.25	0.1	0.1	0.05

performance during forming operations in pre-aged condition together with a giant, dislocation-assisted hardening response, which not only compensates the strength drop of cold-worked AlMg alloys, but even significantly exceeds the paint bake response of new and improved AlMgSi alloys with additions of Zn and Cu [9]. The interactions of alloy composition and proposed processing are discussed based on mechanical testing and detailed microstructural investigation over the processing route via scanning transmission electron microscopy (STEM) and atom probe tomography (APT). The beneficial role of Cu additions is supported by first-principles calculations.

2. Experimental

2.1. Alloy production and thermomechanical treatment

The alloys investigated in this study (see Table 1) are based on EN AW-5182 and modified with additions of Zn and Zn+Cu denoted as 5182-Zn and 5182-ZnCu, respectively, and were produced by vacuum-induction melting, homogenization (470°C/24h), hot and cold rolling on laboratory scale [56]. The commercial base alloy was chosen due to its beneficial forming performance and its wide acceptance and application in automotive body parts.

Samples were subsequently treated according to our proposed thermomechanical treatment strategy (shown in Table 2), consisting of solution heat treatment/water quenching, short-term pre-aging (1st aging stage), pre-deformation (2%) and final paint bake treatment (2nd aging stage). The parameters for paint-baking were chosen in accordance with industrial practice for comparability. The processing sequence was performed for both alloys without (TMT 1) and with applied pre-deformation (TMT 2) before the last aging stage for investigating the effect of pre-strain. To highlight the response of the investigated alloys to the applied treatment strategies, samples of unmodified EN AW-5182 (see Table 1) were produced on the same laboratory scale and similar treated according to the procedures described in Table 2. Note that solution heat treatment and pre-aging were not applied for EN AW-5182. Instead, soft-annealing (1h at 370°C and slow cooling, denoted with suffix "O") was performed on these samples to ensure adequate comparability with the industrial standard.

The chemical composition of the investigated alloys was determined by optical emission spectroscopy (OES). Each composition in Table 1 represents an average of 50 individual measurements (5 measurements per slab, 10 slabs per alloy) on a milled slab surface

after homogenization. The error for Mg and Zn is < 0.1 wt.% and < 0.05 wt.% for all other elements.

In each condition three samples (manufactured in accordance with EN ISO 6892-1:2014) were mechanically tested (and pre-strained if applied) on a Zwick/Roell BT1-FR100THW.A2K tensile testing machine equipped with a 50 kN load cell. For clarification, true stress-strain curves were fitted iteratively starting from the beginning of plastic deformation ($Rp_{0.2}$) up to necking (A_g) by the least square method utilizing a model approach [57] based on the Taylor equation and an extended Kocks-Mecking dislocation model. Fitted true-stress strain curves were then used for calculating the corresponding strain hardening rate (SHR).

2.2. Scanning transmission electron microscopy (STEM)

Thin-foils for STEM investigations were prepared by grinding the alloys to a thickness of approx. 100 μm. Punched out 3-mm discs were further processed by twin jet electro-polishing using a solution of 25% nitric acid in methanol at a temperature range of −16°C to −20°C and a voltage range of 10 V to 20 V. Note that for both pre-aged (PA) and pre-deformed (PS) conditions (see Table 2) grinding, punching and electro-polishing was performed within 4h after the last processing step to account for potential natural aging [58]. Samples for in-situ STEM heat treatments were additionally processed as described in [59].

Electron microscopy was carried out using a Thermo Fisher ScientificTM Talos F200X scanning transmission electron microscope. For statistic investigations high angle annular dark field (HAADF), bright field (BF-TEM), selected-area electron diffraction (SAED) and energy-dispersive X-ray spectroscopy (EDX) measurements were conducted. For in-situ STEM heat treatments a Protochips FUSION MEMS chip-based holder was utilized. Samples in pre-deformed condition (PS) were subjected to heating up to the paint bake temperature of 185°C (heating rate 60°C/s) and holding at this temperature for up to 3h before cooling to room temperature (25°C) at similar rate. Image sequences were acquired using a bright field (BF-STEM) detector. For more details the reader is referred to [59].

Precipitate number densities were calculated by dividing the areal density (extracted from particle analysis) by an average thickness of 50 nm as found in similar samples by EELS/EFTEM [60]. Statistical particle analysis was performed on BF-TEM images (for condition PA) and binary EDX mappings of Zn (for conditions TMT 1/TMT 2) using ImageJ (Version 1.52p) [61].

2.3. Atom probe tomography (APT)

Blanks ($0.7 \times 0.7 \times 20$ mm³) for APT analysis were cut from untested tensile testing specimens in TMT 1 and TMT 2 condition. For pre-aged (PA) samples, blanks were cut from cold-rolled sheet before the heat treatment and instantly processed afterwards by two-step electro-polishing (1st step: 25% HNO_3 in methanol, 2nd step: 2% $HClO_4$ in 2-butoxyethanol) to account for potential natural aging [58]. APT experiments were performed within 24h after electro-polishing in voltage mode with a pulse fraction of 20%, a

Table 2
Parameters of the thermomechanical treatments applied for this study. Process sequence from left to right.

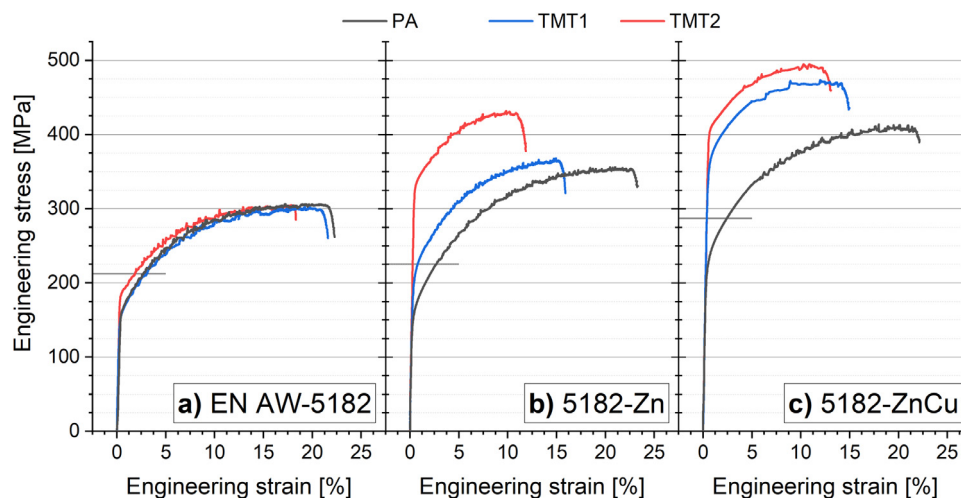| Condition	Solution heat treatment	1st stage Pre-aging	Pre-deformation	2nd stage Paint bake treatment
PA	465°C/35 min + WQ	100°C/3h		
PS	465°C/35 min + WQ	100°C/3h	2%	
TMT 1	465°C/35 min + WQ	100°C/3h	-	185°C/20 min
TMT 2	465°C/35 min + WQ	100°C/3h	2%	185°C/20 min

WQ: water quenching.

Fig. 1. Stress-strain curves of EN AW-5182-O (a) 5182-Zn (b) and 5182-ZnCu (c) after PA (black line), TMT 1 (blue line) and TMT 2 (red line). The grey horizontal lines indicate the deformation (2%) applied on pre-aged samples before the paint bake stage of TMT 2. (For interpretation of the references to color in this figure, the reader is referred to the web version of this article.)

frequency of 200 kHz and a detection rate of 1% at a temperature of $-243°C$ on a LEAP 3000 X HR.

For APT solute analysis the $^{24}Mg^{2+}$, $^{25}Mg^{2+}$, $^{26}Mg^{2+}$, $^{24}Mg^+$, $^{25}Mg^+$, $^{26}Mg^+$, $^{63}Cu^+$, $^{65}Cu^+$, $^{64}Zn^+$, $^{66}Zn^+$, $^{67}Zn^+$, $^{68}Zn^+$, $^{70}Zn^+$, $^{64}Zn^{2+}$, $^{66}Zn^{2+}$, $^{67}Zn^{2+}$, $^{68}Zn^{2+}$ and $^{70}Zn^{2+}$ peaks were used. The reconstruction was built by calibrating the field factor k_f with the observed atomic interlayer spacing and the image compression factor with the observed angles of chosen poles [62] within the commercial program IVAS 3.6.12.

The cluster search was performed based on a threshold density calculated via Voronoi volume [63] for Zn (in alloy 5182-Zn) and Zn+Cu (in alloy 5182-ZnCu) as core atoms. Number densities were calculated by the number of features (detected by cluster search) divided by the analyzed volume of the corresponding APT data set. The volume was measured via the built-in function "AlphaShape" in MATLAB^{TM} [64]. For error estimation in experimental number density both counting errors [65] and errors in volume analysis of the corresponding datasets were taken into account and is described in detail in the Appendix.

Composition of solute clusters was extracted from cluster search data by customized scripts [66]. Matrix composition was calculated at regions of interest (ROI) within APT datasets by subtracting the respective number of atoms (e.g. Mg, Zn, Cu) found in clusters and/or precipitates (detected by the cluster search algorithm) from the respective total number of atoms of the ROI. The corresponding error margin for solute clusters and matrix was calculated as described in [67]. Proxigram data used for quantification of precipitate composition (as shown in Fig. 13 in the Appendix) was exported via IVAS 3.6.12 based on iso-density surfaces (4.11 atoms/nm^3) of Mg and Zn atoms.

For radial distribution function (RDF) analysis, the formalism described in previous works [58,68] was used. Al, AlH$_1$ and AlH$_2$ are counted as Al, further only Mg, Zn and Cu atoms are counted for composition calculation.

For morphology determination, semi-axes (L$_1$, L$_2$ and L$_3$, where L$_1 \geq$ L$_2 \geq$ L$_3$) of best-fit ellipsoids [69] were extracted from cluster search data and plotted in terms of ellipsoid volume over aspect ratio (L$_2$/L$_1$) and oblateness (L$_3$/L$_2$) for each feature. For comparison, the average feature size was evaluated in terms of the Guinier radius, which was determined from log-normal-fitting functions of the size distribution of GPI-zones for pre-aged conditions (PA) and calculated by the arithmetic mean for precipitates in TMT 1 and TMT 2 condition due to insufficient fitting.

2.4. Density functional theory (DFT) calculations

DFT results were computed using Quantum Espresso (QE) [70], using the GGA-PBE [71] exchange-correlation functional with a 544 eV energy cutoff, a Monkhorst-Pack [72] kpoint grid consistent with a 20 × 20 × 20 mesh for a 4.04 Å^3 conventional FCC cell (80 kpoints/Å), along with 0.6 eV of Methfessel-Paxton smearing. The Al and Mg pseudopotentials were chosen from the solid-state pseudopotential (SSSP) library [73]. The Cu pseudopotential of Dal Corso [74] was used as it was found to have a better accuracy and reduced computational cost. For the solute energies the Zn potential of the SSSP was used, however, at 20 valence electrons, it was found to be prohibitively expensive for calculations on the η' phases. For the η' and T phases, the Zn potential of Dal Corso [74] with 11 valence electrons was used. Studies for 1st and 2nd nearest neighbor Zn pairs and (111) and (100) plane clusters show differences within 5 meV to the SSSP potential.

3. Results

3.1. Mechanical behavior

Stress-strain curves of the investigated alloys are shown in Fig. 1 for each condition. The associated yield strength as well as their change with thermomechanical treatment are shown in Table 3.

In their dedicated forming condition (after the 1st aging stage, PA) both 5182-Zn (Fig. 1b, black line) and 5182-ZnCu (Fig. 1c, black line) exhibit increased work hardening and a later onset of serrated flow without deterioration of elongation as compared to EN AW-5182-O (Fig. 1a, black line). The strength level of 5182-ZnCu is significantly higher (226 MPa) compared to 5182-Zn (157 MPa) and EN AW-5182-O (159 MPa). This observation is consistent with previous findings by Geng et al. [35] but the strength level is significantly lower compared to reported values due to the shorter preaging time and, therefore, more beneficial for forming operations. By plotting the strain hardening rate (SHR) over true stress (Kocks-Mecking-Plot, see Fig. 2b) for fitted true stress-strain curves (for details see Section 2) of EN AW-5182-O (black line), 5182-Zn (blue line) and 5182-ZnCu (red line) shown in Fig. 2a, a clear shift to higher SHR and a flattening of the curve for the both 5182-Zn and 5182-ZnCu is evident. This can be linked to enhanced dislocation

Table 3

Change in yield strength of the investigated alloys according to the applied thermomechanical treatments.

Rp$_{0.2}$ [MPa]	TMT 1			TMT 2		
	EN AW-5182	5182-Zn	5182-ZnCu	EN AW-5182	5182-Zn	5182-ZnCu
after PA	159 ± 4*	157 ± 6	226 ± 5	159 ± 4	157 ± 6	226 ± 5
after pre-deformation**	-	-	-	212 ± 2	225 ± 1	287 ± 1
after TMT	159 ± 6	204 ± 5	353 ± 16	188 ± 2	335 ± 12	410 ± 5
THR[a]	**0**	**47**	**127**	**29**	**178**	**184**
Hardening component due to deformation	-	-	-	-53	-68	-61
Softening component due to recovery	-	-	-	24	24	24
sPBR[b]	**0**	**47**	**127**	**0**	**134**	**147**

* corresponds to soft-annealed condition (suffix "O").
** corresponds to Rm-value at 2 % deformation of PA, see grey horizontal lines in Fig. 1.
[a] total hardening response.
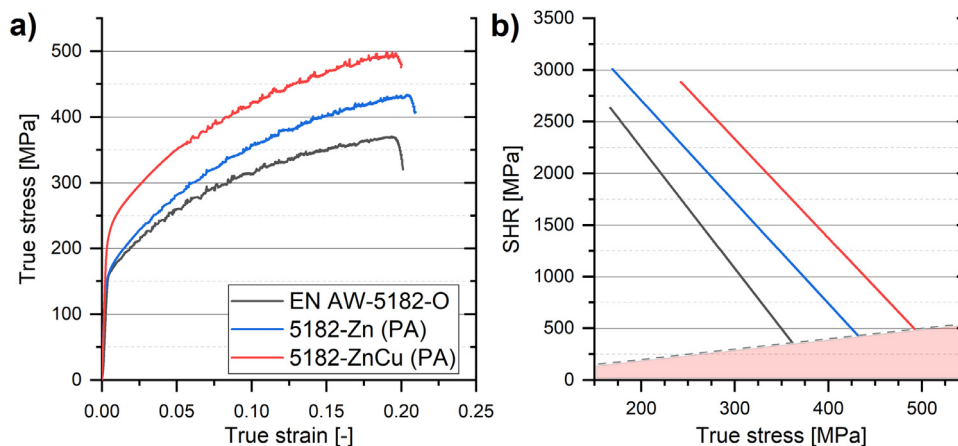[b] sole paint bake response.

Fig. 2. True stress-strain curves of the investigated alloys in their dedicated forming condition (a) Kock-Mecking-plots [76] corresponding to the fitted true stress-strain curves (b). The dashed grey line represents the Considère criterion. (For interpretation of the references to color in this figure, the reader is referred to the web version of this article.)

formation and inhibited dislocation annihilation corresponding to enhanced stretch-formability [34,75–77].

Applying a paint bake treatment without pre-deformation (TMT 1), the total hardening response (THR, calculated by subtracting the yield strength after the 2nd aging stage by the yield strength after the 1st aging stage) of 47 MPa is only minor in 5182-Zn (Fig. 1b, blue line) and reaches a yield strength of 204 MPa. In contrast, 5182-ZnCu exhibits a strongly pronounced total hardening response of 127 MPa leading to a yield strength of 353 MPa (Fig. 1c, blue line). The elongation at fracture of both alloys is still close to 15% regardless of the higher strength level. For the reference alloy EN AW-5182 the same treatment (TMT 1) does not show any effect (Fig. 1a, blue line), which is not surprising due to the total absence of any precipitate-forming solutes.

In the case of TMT 1 treatment, the total hardening response is similar to the sole paint bake response (sPBR). This differentiation is necessary to account for the effect of applied pre-strain in TMT 2, which is now discussed.

After applying the paint bake on pre-strained samples (TMT 2), a giant total hardening response of 178 MPa and 184 MPa are evident for 5182-Zn (Fig. 1b, red line) and 5182-ZnCu (Fig. 1c, red line) reaching a yield strength of 335 MPa and 410 MPa, respectively. Additionally, their elongation at fracture is higher than 10% and the work hardening is still significant despite their high strength.

To adequately compare the hardening response during the thermomechanical treatments without pre-deformation (TMT 1) and with pre-deformation (TMT 2), contributions from hardening by pre-straining and softening by dislocation annihilation (recovery) during paint bake treatment need to be taken into account for TMT 2. While the hardening component can be easily calculated

for each alloy, the softening component is harder to access. This information can be extracted by comparing the effect of the different treatment strategies on the EN AW-5182 samples (Table 3). Here the yield strength increases from 159 MPa to 212 MPa via pre-deformation (indicated by grey horizontal lines in Fig. 1a) exhibiting a strain hardening component of 53 MPa. After paint baking for 20 minutes at 185°C the strength dropped down to 188 MPa. Since no precipitate-forming elements are present in this alloy and the sPBR in EN AW-5182 is therefore negligible, the stress drop from 212 MPa to 188 MPa is associated with a recovery component of 24 MPa. This value can now be used as a rough approximation to account for the recovery-induced softening in 5182-Zn and 5182-ZnCu although it should be noted that the recovery may be somewhat lower due to the presence of precipitates. If the work-hardening component of the modified alloys (68 MPa for 5182-Zn, 61 MPa for 5182-ZnCu) is reduced by the recovery value of 24 MPa, we obtain the net dislocation hardening. If this amount is deducted from the TMT 2 hardness increase, we obtain the values for the sole paint bake response (sPBR) of 134 MPa for 5182-Zn and 147 MPa for 5182-ZnCu.

The results from mechanical testing can be summarized by the following observations: (i) While both alloys offer beneficial mechanical properties including high uniform elongation, increased work hardening and delayed onset of serrated flow after short-term pre-aging (PA), the Cu-containing 5182-ZnCu exhibits additionally a slightly higher strength level. (ii) Applying a paint bake treatment without pre-deformation (TMT 1) 5182-Zn shows a total hardening response of only 47 MPa while the yield strength of 5182-ZnCu rises by 127 MPa, indicating a beneficial role of Cu. (iii) If 2% pre-deformation is applied after the pre-aging and
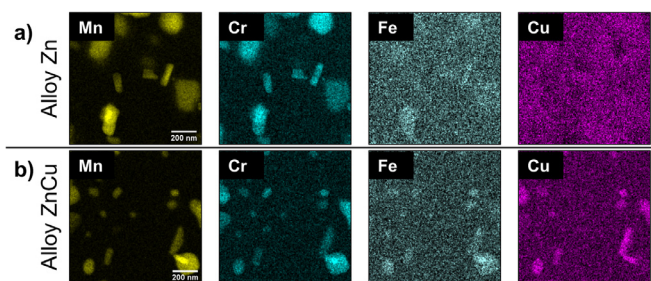
Fig. 3. EDX mappings of Mn, Cr, Fe and Cu in dispersoids. Images were acquired in PA condition for 5182-Zn (a) and 5182-ZnCu (b). Scale bars in the EDX mapping of Mn apply also for other EDX mappings.

Table 4
Matrix composition according to APT analysis in at.%.

Condition	Alloy	Al	Mg	Zn	Cu
PA	5182-Zn	93.9 ± 0.01	4.7 ± 0.01	1.4 ± 0.01	0.0 ±0.01
	5182-ZnCu	93.4 ± 0.01	4.9 ± 0.01	1.5 ± 0.01	0.2 ± 0.01
TMT 1	5182-Zn	94.6 ± 0.02	4.2 ± 0.02	1.2 ± 0.01	0.0 ± 0.01
	5182-ZnCu	95.4 ± 0.04	3.9 ± 0.04	0.6 ± 0.01	0.1 ± 0.01
TMT 2	5182-Zn	95.9 ± 0.01	3.4 ± 0.01	0.7 ± 0.01	0.0 ± 0.01
	5182-ZnCu	96.0 ± 0.03	3.5 ± 0.03	0.4 ± 0.01	0.1 ± 0.01

before the paint bake treatment (TMT 2) a giant total hardening response of 178 MPa and 184 MPa can be observed in 5182-Zn and 5182-ZnCu, respectively. Even after accounting for hardening by pre-deformation and softening by recovery during the paint bake treatment, the hardening response is higher by 87 MPa for 5182-Zn and 20 MPa for 5182-ZnCu compared to TMT 1, indicating a boosting effect of pre-strain on artificial aging.

In light of that findings the following results are presented with a focus on the role of chemical composition and pre-strain and will be thoroughly discussed in section 4.

3.2. Evolution of the microstructure

To understand the observed differences in mechanical properties, the microstructures of 5182-Zn and 5182-ZnCu were examined over the treatment sequence by using APT and several STEM techniques. Before evaluating the hardening precipitates in detail, the condition of dispersoids and the matrix are thoroughly assessed to avoid misinterpretation.

3.2.1. Dispersoids and matrix

In Fig. 3 EDX mappings of dispersoids are shown for 5182-Zn and 5182-ZnCu. Note that EDX mappings of dispersoids were acquired in PA condition only, since dispersoids are not affected by the subsequent low temperature treatments. The observed aggregates of Mn, Cr and Fe in 5182-Zn are inherited from the industrial base alloy EN AW-5182 and are essential to maintain the good forming performance attributed to the base alloy due to their effect on grain structure development.

According to thermodynamic calculations [78] these aggregates can be identified as (or a mixture of) $Al_6(Mn,Fe)$, $Al_{11}(Cr,Mn)_2$ and Al_9Mn_2Si (with some solubility for Fe). Even though the same dispersoid-forming elements in similar quantity are present in 5182-ZnCu, these aggregates also incorporate Cu beside Mn, Cr and Fe (see Fig. 3b). This observation can be confirmed by including Cu in the thermodynamic calculations revealing the possibility of $Al_7(Mn,Fe,Cu)_3$ formation, suggesting a reduced Cu-content in the matrix at solution heat treatment temperature (465°C) [78]. A detailed investigation on the landscape of dispersoids would exceed the scope of this study, but the incorporation of Cu into dispersoids, which usually form at early stages of the processing chain (homogenization, hot rolling), obviously limits the availability of Cu at later thermomechanical treatments to some extent.

The matrix content of the main precipitate-forming solutes in each alloy and condition is shown in Table 4 and will be used to assess the level of solute depletion (loss of supersaturation) over the applied thermomechanical treatments.

After applying TMT 1 on 5182-Zn the supersaturation of Mg and Zn (the two major constituents of the expected hardening phase beside Al) decreased only by 0.5 at.% and 0.2 at.%, respectively, while the solute depletion was higher after TMT 2 ($\Delta Mg = 1.3$ at.%,

$\Delta Zn = 0.7$ at.%). In 5182-ZnCu the solute content of Mg and Zn decreased by 1.0 at.% and 0.9 at.%, respectively, after TMT 1, but the depletion is also more pronounced after TMT 2 ($\Delta Mg = 1.4$ at.%, $\Delta Zn = 1.1$ at.%).

The remaining supersaturation of Mg and Zn in the matrix of both alloys is lower after TMT 2 than after TMT 1 indicating that a reduction of supersaturation (or in other words precipitation) is promoted by pre-deformation. Additionally, the remaining matrix solute content is lower in 5182-ZnCu compared to 5182-Zn after both treatments, indicating an enhanced precipitation of hardening phase if Cu is present. Also, the matrix Cu-content in 5182-ZnCu, which was already reduced by dispersoid formation, is halved during both treatments, indicating that 0.1 at.% Cu was consumed by precipitate formation.

To account for any effects on the smallest scale, the normalized (divided by random) radial distribution functions (RDF) for Mg-Mg, Zn-Zn, Mg-Zn, Cu-Cu, Mg-Cu and Zn-Cu interactions (the latter three only for 5182-ZnCu) were calculated at ROIs where no precipitates were present, and are plotted in Figs. 14 and 15 in the Appendix for PA and TMT 1/TMT 2, respectively. For a random distribution of solute atoms in the matrix, the normalized RDFs would exhibit values of 1. Values larger than one (> 1) account for non-random distribution of solutes, which indicates the existence of clusters.

After pre-aging (PA), non-random distribution of solutes is evident for both alloys but more pronounced in 5182-ZnCu (Fig. 14, yellow line). If Cu is present in the alloy not only interactions with Cu-participation (Cu-Cu, Mg-Cu and Zn-Cu) are observed, but also Mg-Mg, Zn-Zn and Mg-Zn interactions are more distinct. The higher solute content of the matrix in 5182-ZnCu might contribute to the increased interaction of Mg-Mg, Zn-Zn and Mg-Zn but cannot account for the full enhancement, indicating indeed a stimulating effect of Cu on the cluster formation.

Interestingly, such indications are also present in 5182-Zn after TMT 1 (Fig. 15, black line) which are absent in 5182-ZnCu (Fig. 15, blue line) and largely absent in both alloys after TMT 2 (Fig. 15, red and green lines). This effect is especially pronounced for the Zn-Zn interaction (Fig. 15b) and a bit weaker for Mg-Zn (Fig. 15d), which is consistent with the higher remaining solute content of Mg and Zn in 5182-Zn after TMT 1 (Table 4) and might be attributed to fast secondary natural aging after the final paint bake treatment and prior to APT sample preparation.

So, if Cu is present in the alloy or pre-strain was applied before the paint bake treatment, the solute content of the matrix after the final aging stage is significantly lower and no solute interaction can be observed. This implies that more solutes have participated in the formation of precipitates during the applied heat treatments. On the contrary, in absence of Cu or pre-deformation, precipitation is somehow inhibited and solute aggregates remain in the matrix in addition to precipitates.

3.2.2. Precipitates

In age-hardenable aluminum alloys, the dominating hardening mechanism is precipitation strengthening. Precipitates act as obstacles and inhibit dislocation motion through the matrix. The

Table 5

Guinier radius, semi-axes and number densities of clusters and precipitates for each alloy and condition. A detailed overview on morphology distribution can be additionally found in Fig. 16 in the Appendix. For validation number densities have been evaluated from both TEM and APT data. As can be seen both methods show consistent results. For more details, the reader is referred to section 2.

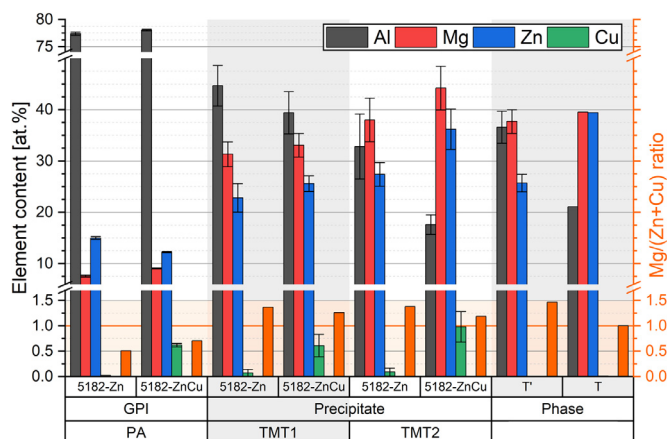| Alloy	Condition	Guinier radius [nm] APT	L_1 [nm]	L_2 [nm]	L_3 [nm]	Number density [10^{23} m^{-3}]	Number density [10^{23} m^{-3}] STEM
5182-Zn	PA	1.7 ± 0.4	2.5 ± 0.8	1.5 ± 0.4	0.9 ± 0.2	3.5 ± 0.7	4.1 ± 0.2
	TMT 1	5.4 ± 2.0	8.4 ± 3.5	3.6 ± 0.9	1.7 ± 0.2	0.3 ± 0.1	0.2 ± 0.1
	TMT 2	3.7 ± 1.3	5.4 ± 2.1	2.7 ± 1.0	1.7 ± 0.5	0.9 ± 0.3	0.7 ± 0.1
5182-ZnCu	PA	2.1 ± 0.4	3.3 ± 1.2	1.9 ± 0.5	1.1 ± 0.4	5.0 ± 0.6	5.5 ± 0.6
	TMT 1	2.8 ± 0.8	3.7 ± 1.3	2.5 ± 0.6	1.7 ± 0.5	1.6 ± 0.2	1.7 ± 0.6
	TMT 2	3.1 ± 2.1	4.5 ± 3.2	2.4 ± 1.5	1.3 ± 0.8	1.2 ± 0.2	1.0 ± 0.1

Fig. 4. Elemental composition of GPI/precipitates for each alloy and condition. Data corresponding to T'- [28] and T-phase [29,42] is shown for comparison reasons. GPI composition was assessed from cluster search, while precipitate composition was evaluated from proxigram data (for details see section 2).

Fig. 5. 3D-elemental maps from APT, BF-TEM images, DPs (acquired along the ⟨001⟩ zone axis of the aluminum matrix) and EDX mappings of 5182-Zn for PA (a), TMT 1 (b) and TMT 2 (c). In the APT reconstruction pink dots correspond to Mg-atoms and grey dots correspond to Zn-atoms. For better visibility of the GPI-zones in PA condition the APT reconstruction is additionally shown without matrix atoms and increased dot size. Scale bars in the EDX mapping of Mg apply also for other EDX mappings.

hardening capability of precipitates is affected by their chemical constitution, but also by geometrical aspects like size, number density and morphology. To understand the observed differences in mechanical behavior (Fig. 1) precipitates in each alloy and condition have been thoroughly assessed by APT and STEM.

Chemical composition of precipitates was evaluated from cluster search data for small solute clusters in the matrix as well as from proxigram data for larger precipitates with a higher degree of development (for details see Section 2). While cluster search data only gives an approximation for the average composition of the whole detected solute agglomerate, proxigram data offers a more detailed insight in the center of the precipitates and limits experimental errors. Since Al is a strong indicator for the development status of T-phase precipitates, their evolution is discussed based on proxigram data (similarly conducted by Bigot et al. [28]) in terms of element composition and corresponding Mg/(Zn+Cu) ratio (as shown in Fig. 4). While GPI-zones after PA consist of almost 80 at.% Al and only minor amounts of Mg and Zn indicating an early development stage, precipitates after TMT 1 and TMT 2 exhibit a chemical composition significantly closer to compositions reported for intermediate T' [28] and equilibrium T-phase [29,42].

To account for geometrical aspects, the size, morphology and number density of precipitates has been extracted from APT data for each alloy and condition as shown in Table 5. Number densities were additionally evaluated from STEM data for validation and were found to agree with APT results. As can be seen from Table 5, the semi-axes of clusters and precipitates (L_1, L_2 and L_3, where $L_1 > L_2 > L_3$) exhibit a significant variation not only between investigated conditions but also within one condition, which is even more obvious in the detailed morphology determination for each cluster and precipitate in Fig. 16 in the Appendix. However, the size evo-
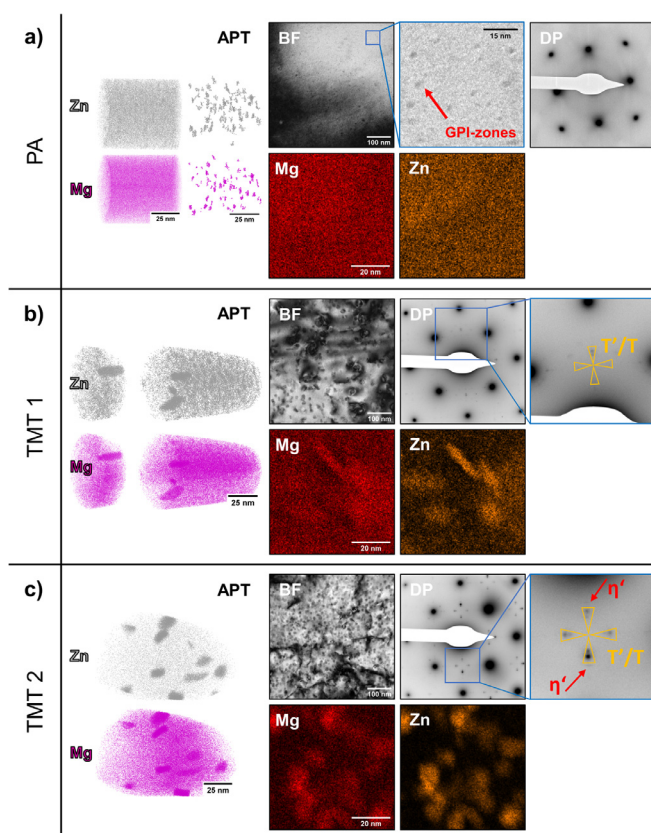
lution of precipitates will be discussed, for clarification, in terms of their Guinier radius. For details the reader is referred to section 2.

For easier interpretation, results are now discussed in detail for each alloy individually. Note that quantitative results in the following sections correspond to APT data.

3.2.2.1. Hardening phase in 5182-Zn. After pre-aging of 5182-Zn (Fig. 5a, Clip A in supplementary material) the bright field image (BF-TEM) reveals homogeneously dispersed dark spots (as representatively indicated by the red arrow) in the Al-matrix, which agrees well with the Mg/Zn-containing solute aggregates found by APT measurements. These early stage precursors exhibit an average Guinier radius of 1.7 nm and are primarily present in a distorted globular shape (Fig. 16a in the Appendix). They exist at a number density of 3.5×10^{23} m^{-3} (Table 5) and show a low degree of

chemical development (Fig. 4), with an average Mg/(Zn+Cu) ratio close to 0.5. In contrast to results from APT, aggregation of Mg and Zn could not be observed with EDX analysis at this stage, which is attributed to both the detection limit and spatial resolution of this technique in combination with a likely dissolution of the small precursors due to electron-irradiation introduced during the measurement itself. In agreement with generally accepted electron-beam contrast mechanisms [79,80], the lack of extra reflection spots except those of the Al-matrix spots in the corresponding diffraction pattern (DP), results from APT, and the nomenclature proposed by Hou et al. [49] we term the dark spots/clusters as GPI-zones.

After applying the paint bake treatment without pre-deformation (Fig. 5b) precipitates in a number density of 0.3×10^{23} m^{-3} are observed. These large and mainly lath- and rod-shaped precipitates (Fig. 16c in the Appendix) exhibit an average Guinier radius of 5.4 nm (Table 5) and can be clearly identified by the aggregation of Mg and Zn in the 3D-reconstruction of the APT tips as well as in the EDX mappings and the extra reflection spots in the DP as T-phase or its precursors [28]. According to APT data (Fig. 4) the chemical composition of these precipitates is different from the clusters found in 5182-Zn after PA and shows higher levels of both Mg and Zn and a lower level of Al.

Additionally, the Mg/(Zn+Cu) ratio increased to 1.4 in favor of a higher Mg contribution suggesting that growth of precipitates is governed by incorporation of Mg and to lesser extent by consumption of Zn. This indicates a higher degree of development compared to the PA condition. Even though the equilibrium composition [29,42] (denoted T in Fig. 4) is not reached at this stage, the observed composition has almost reached the composition of the intermediate T' reported by Bigot et al. [28], identifying them as precursors of the T-phase (T').

If 2 % pre-strain is applied before the 2nd aging stage (Fig. 5c) precipitates exist at a number density three times higher $(0.9 \times 10^{23}$ m$^{-3})$ and with smaller average size (Guinier radius 3.7 nm, Table 5) compared to TMT 1. The majority of precipitates are significantly less elongated and more globular (Fig. 16e in the Appendix) and their chemical composition (Fig. 4) shows an increased incorporation of Mg and Zn and a lower amount of Al in the precipitates, clearly identifying them as intermediate T'-phase. The Mg/(Zn+Cu) ratio is affected by pre-straining only to a minor extent. Interestingly, the magnified diffraction pattern (DP) in this condition shows fainted spots located at the 1/3 and 2/3 ⟨022⟩ Al position beside the matrix and the T-phase spots, possibly η'-phase [81]. Due to the fact that non-random distribution of solutes in the matrix was not detected after TMT 2, it is assumed that pre-straining affects the development of hardening phase and that precursors with η'-phase or η'-phase-like structure might be involved in the formation of T-precipitates. This issue will be further addressed in a later section.

3.2.2.2. Hardening phase in 5182-ZnCu. In the pre-aged condition (Fig. 6a, Clip B in supplementary material), GPI-zones (indicated by the red arrow) at a number density of 5.0×10^{23} m^{-3} were identified in 5182-ZnCu based on STEM and APT results as mentioned before. These slightly larger GPI-zones (Guinier radius 2.1 nm, Table 5) exhibit predominately a distorted globular morphology and occupy a larger volume within the matrix compared to 5182-Zn in the PA condition (Fig. 16b in the Appendix). Also similar to 5182-Zn, the corresponding DP does not show extra reflections beside the Al-matrix and a clear aggregation of solutes (Mg, Zn and Cu) was also not observed in the EDX mappings of 5182-ZnCu, possibly due to the above stated experimental limits of this method.

APT data revealed that GPI-zones present in 5182-ZnCu after PA (Fig. 4) exhibit a similar total solute content (Mg+Zn+Cu) compared to the non-Cu-containing alloy but here the Mg content
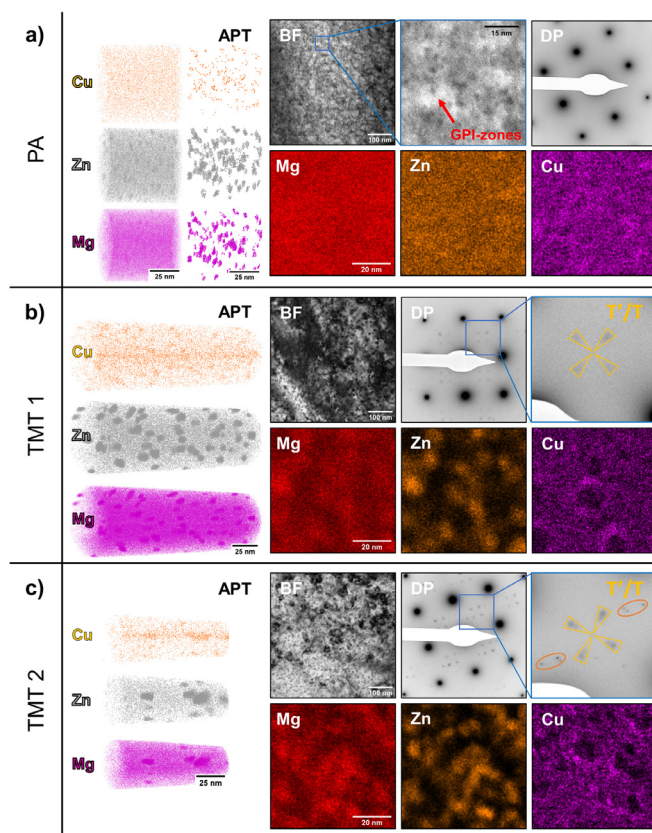

Fig. 6. 3D-elemental maps from APT, BF-TEM images, DPs (acquired along the ⟨001⟩ zone axis of the aluminum matrix) and EDX mappings of 5182-ZnCu for PA (a), TMT 1 (b) and TMT 2 (c). In the APT reconstruction pink dots correspond to Mg-atoms, grey dots correspond to Zn-atoms and orange dots correspond to Cu-atoms. For better visibility of the GPI-zones in PA condition the APT reconstruction is additionally shown without matrix atoms and increased dot size. Scale bars in the EDX mapping of Mg apply also for other EDX mappings.

exceeds the level of Zn-incorporation. Additionally, they incorporated approximately 0.6 at.% Cu, which is 0.4 at.% higher compared to the matrix (see Table 4) and, therefore, is also significant due to the fact that some Cu has been already consumed by dispersoids (Fig. 3b). Despite the (although small) Cu-enrichment the Mg/(Zn+Cu) ratio of 0.7 is higher compared to GPI-zones in 5182-Zn (0.5), suggesting a higher degree of chemical development. Interestingly, the Mg/(Zn+Cu) ratios observed are close to reported values for η'-precipitates [82], which will be addressed in later sections.

After the paint bake of 5182-ZnCu without pre-deformation (TMT 1), small globular precipitates at a number density of 1.6×10^{23} m^{-3} and an average Guinier radius of 2.8 nm (Table 5) are present in the aluminum matrix (Fig. 6b and Fig. 16d in the Appendix). The smaller precipitate size and the more than five-times higher number density accounts well for the higher hardening response of 5182-ZnCu (Fig. 1c) compared to 5182-Zn (Fig. 1b) in similar condition. While EDX mappings of Mg and Zn reveal a clear aggregation of both elements, Cu incorporations cannot be observed presumably due to a low amount of incorporation and the limit of detection. Quantitative analysis of precipitate composition from APT data (Fig. 4) exhibits a Cu-enrichment of 0.6 at.% in average, six times higher compared to the matrix (0.1 at.%). The levels of Al, Mg and Zn in the precipitates identify them as intermediate T' and indicate a higher degree of chemical evolution towards the equilibrium condition compared to 5182-Zn after TMT 1. The Mg/(Zn+Cu) ratio remains almost unaffected by the presence

of Cu, showing a level of 1.3 and additional diffraction spots beside matrix and T-phase spots are absent.

According to STEM results (Fig. 6c), 2% pre-deformation before the paint bake treatment (TMT 2) seems to have an only minor effect on the size and morphology of the precipitates in 5182-ZnCu but a closer look on the morphology distribution (shown in Fig. 16f in the Appendix) reveals a larger average precipitate size (even though less pronounced in terms of the Guinier radius of 3.1 nm, Table 5) and a significantly higher degree of elongation compared to TMT 1 condition. Interestingly, their number density after TMT 2 is lower (1.2×10^{23} m^{-3}) but the chemical composition of the precipitates exhibits the most advanced development toward equilibrium T (Fig. 4) and the highest level Cu-incorporation (1.0 at.%), which is assumed to affect the strengthening ability of the hardening phase and will be discussed in Section 4. The additional diffraction spots present (indicated by orange circles in the DP Fig. 6c) have been identified as multiple reflections of T-phase but, in contrast to 5182-Zn in similar condition, no reflections corresponding to η'-phase or η'-phase-like structures beside matrix and T-phase are observed.

3.3. DFT calculations

As can be seen from our experimental findings (Fig. 1 and Table 3) a beneficial effect of Cu on the overall hardening response is evident. GPI-zones after PA are present at a higher number density and at a larger size in the presence of Cu. Also, solute clusters and η'-phase diffraction spots are absent in 5182-ZnCu after both TMT 1 and TMT 2 (Fig. 6) while the corresponding precipitates show an enhanced chemical development (Fig. 4). To examine the role of Cu in early stage clustering and precipitation, we have performed targeted first-principles Density Functional Theory (DFT) studies that reveal some beneficial effects of Cu.

Since it has been well-established that the terminal precipitate in the present alloys is the T-phase, we examine the energetics of Cu substitution for this structure. In addition, particular attention is also paid to the potential stabilization of surrogate η'-type phases. Based on indications for η'-involvement in the DP of 5182-Zn after TMT 2 (Fig. 5c) as well as the Mg/(Zn+Cu) ratio observed in GPI-zones of 5182-ZnCu after pre-aging (Fig. 4) it seems reasonable to assume that such smaller structures (18 atoms in the unit cell of η') are easier to from compared to T-phase super cells (162 atoms per unit cell), especially at the earlier stages of aging. For easier readability interpretation/discussion of the results is directly included in this section.

We first examine solute-solute pairs and triplets of Mg, Zn, and Cu embedded in a surrounding Al matrix to determine if Cu provides any benefit or detriment to the initial aggregation of solutes into cluster. We concentrate on 2- and 3-atom clusters containing at most one Cu atom because the entropy cost of additional localized Cu atoms is too high at c_{Cu} = 0.25 at.% (for first neighbor, approximately -kT ln(12c) ~144 meV per additional Cu atom) relative to any gains in binding energies. As shown in Fig. 7, for solute-solute first-neighbor pairs in the FCC$_{Al}$ lattice, Mg-Zn has the strongest binding energy (-38 meV), followed by Zn-Zn and Cu-Zn (-23 meV). Cu-Mg binding is weaker (-17 meV) and Mg-Mg is unfavorable ($+13$ meV). These are consistent with the major driving force of Mg-Zn binding, while Cu can bind to Zn as well as Zn binds to itself. We also find that vacancy/Cu binding is small (-20 meV) so that Cu does not affect vacancy-mediated diffusion. Cu therefore does not play any special role for creating initial pairs or influencing transport.

For solute triplets, we consider two configurations, corresponding to the smallest possible triplets on the (100) and (111) planes, as shown schematically in Fig. 7. Mg-Zn-Mg (100) and Mg-Zn-Zn (111) triplets have the strongest binding (-102 meV and -98 meV,
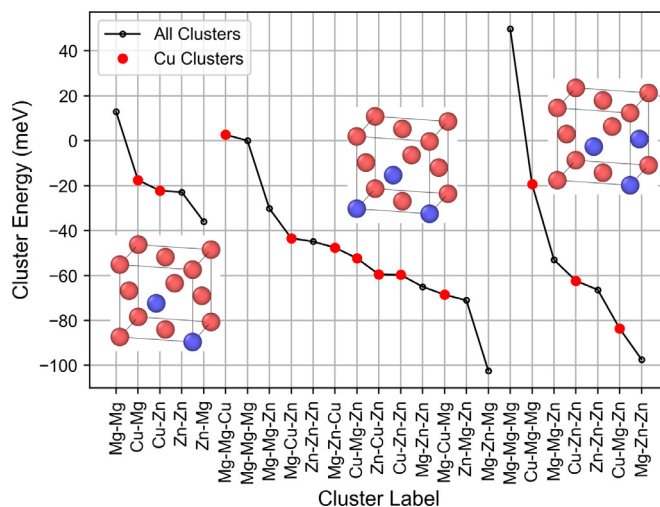

Fig. 7. Cluster energy vs. cluster composition for nearest-neighbor pairs, first/second neighbor triplets on the (100) plane and first neighbor triplets on the (111) plane. For (100) clusters, there are two types of atom sites, and the second atom in the label is the atom with two first neighbors (e.g. for Mg-Zn-Mg, Zn has two Mg first neighbors).

respectively), with no Mg first neighbors, confirming their affinity to form condensed phases (see Fig. 7). Both types of Zn-Zn-Zn triplets are less favorable (-43 meV and -66 meV), demonstrating the preference for Mg-Zn clustering. Both types of Cu-Zn-Zn triplets have essentially the same binding energies as the Zn-Zn-Zn triplets. Furthermore, no Cu-containing triplets are more favorable than the Mg-Zn-Zn (111) and Mg-Zn-Mg (100) triplets, but the Cu-Mg-Zn (111) triplet, which Geng et al. [35] proposed as an early-stage cluster in the present alloy, has a binding energy of -82 meV. Therefore, Cu does not preferentially stabilize the very smallest Mg-Zn clusters, but it can substitute for Zn at very small energy cost.

Based on the indications of η'-involvement as mentioned above we examine the role of Cu within the η'-phase as a potential surrogate precipitate. Following the study by Cao et al. [83], we first consider the η'$_I$-phase that matches well with their HRTEM results (as shown in Fig. 8a). The η'$_I$-phase has an 18-atom unit cell with a composition of Mg$_4$Zn$_6$Al$_8$. Upon introduction of any one of a number of solute substitutions (e.g. Cu for Zn, Zn for Al), DFT computations predict instability of the η'$_I$-phase and transformation into a new phase that we denote by η'$_{IV}$. This transformation, caused by a single solute, is seen in both single-unit (18 atom) cells and $3 \times 2 \times 1$ (108 atom) supercells. When the solute is removed, returning the precipitate to the original composition Mg$_4$Zn$_6$Al$_8$, this new η'$_{IV}$-phase (-76 meV/atom) remains stable and has an energy that is significantly lower than the η'$_I$-phase (-26 meV/atom) which accounts for a total energy reduction of 893 meV per formula unit while also matching well with the HRTEM data (Fig. 8b). Thus, this is a new possible phase for η'. Cao et al. [83] reported huge energy changes upon introduction of solutes into the η'$_I$-phase, but did not recognize that the solutes were triggering this transformation, which was the cause of the large energy change independent of the added solutes.

Introducing solutes into either the η'$_{IV}$-phase or the η'$_I$-phase (while holding the atoms in the η'$_I$-phase at the original lattice sites to prevent the transformation) reveals the role of Cu in stabilizing these phases as shown in Fig. 8c. Specifically, if Cu replaces one Zn atom to create a composition denoted as Mg$_4$(Zn$_5$Cu)Al$_8$, the precipitate energy is lowered by 100 meV. Such an energy change is found for single Cu solutes in both 18 and 108 atom unit cells, indicating that Cu-Cu interactions are negligible. Thus, unlike
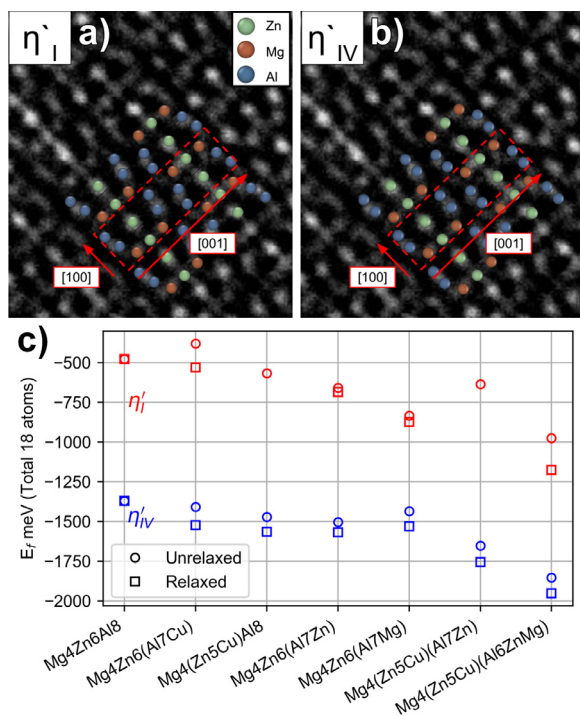
Fig. 8. Overlay of the DFT-computed η'_I (a) and η'_{IV} (b) structures onto the HRTEM image of Cao et al. [83] for the composition Mg$_4$Zn$_6$Al$_8$. The HRTEM was performed on the commercial 7075-alloy, not the alloys studied in the present paper. Mg and Zn atom positions agree well for both η'_I and η'_{IV}. Al atom positions are more challenging to determine from HRTEM, and some regions appear closer to η'_I and others closer to η'_{IV}. (c) Total formation energy E_f for 18-atom η'-precipitates with various solute substitutions starting from the baseline Mg$_4$Zn$_6$Al$_8$ composition. Unrelaxed (circles) and relaxed (squares) energies for both η'_I (red) and η'_{IV} (blue) refer to relaxations of the atom positions holding the unit cell structure fixed, and are shown because some η'_I structures transform to η'_{IV} upon solute substitutions and atomic relaxation. In cases where multiple sites are possible for the solute substitution, the structure with the lowest energy is shown. (For interpretation of the references to color in this figure, the reader is referred to the web version of this article.)

for the pair and triplet clusters, Cu enhances the stability of these η'-phases.

Similarly, consistent with the drive toward increasing Mg and Zn content in the precipitates, the substitution of either Zn or Mg into one of the two types of Al sites, to give a composition Mg$_4$Zn$_6$(Al$_7$Zn) or Mg$_4$Zn$_6$(Al$_7$Mg), also reduces the energy of the precipitate, with the Mg-substitution being particularly favorable, consistent with our experiments showing a steady increase in the Mg content as precipitates evolve (Fig. 4). To examine any interactions among solute substitutions in a single unit cell, we consider 2- and 3- solute substitutions into the same 18 atom unit cells. Substituting a Zn into an Al site and a Cu into the vacated Zn site to form Mg$_4$(Zn$_5$Cu)(Al$_7$Zn) leads to an even lower energy while preserving the Mg/(Zn+Cu) ratio, with the energy close to the sum of those due to the individual solutes. Adding one Mg into one of the Al sites to create the composition Mg$_4$(Zn$_5$Cu)(Al$_6$ZnMg) leads to a further decrease in precipitate energy. All these results lead to the conclusion that dilute Cu additions to η'-phases, but also modified/evolving η'-phases with and without Cu-participation, notably reduce the energies of these phases, which should significantly enhance early stage nucleation of these and similar clusters.

Calculating energies for the terminal T-Mg$_{32}$(Al,Zn)$_{49}$-phase is challenging because there are no site-specific dependencies for Al and Zn but rather Al/Zn sites with unknown occupancy. We have thus created T-phase structures with Al and Zn assigned randomly to the Al/Zn sites so as to attain a final stoichiometry for the equilibrium phase of Mg$_{32}$Zn$_{32}$Al$_{17}$ [29]. The unrelaxed energies of
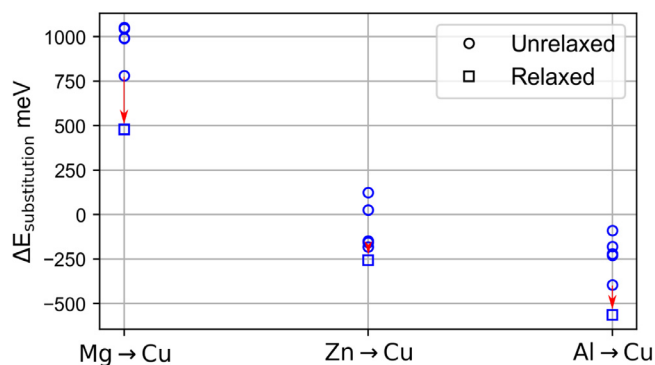

Fig. 9. Substitution energies for replacing Mg, Zn and Al with Cu in the T-phase (Mg$_{32}$Zn$_{32}$Al$_{17}$). The unrelaxed substitutional energies are shown for all the elements for five random sites. The lowest energy site for each substitutional element was selected for atomic relaxation, the resulting energy is also shown. The site with the lowest unrelaxed energy and the energy for that same site after relaxation is shown with a red arrow between the two to help guide the eye. (For interpretation of the references to color in this figure, the reader is referred to the web version of this article.)

three random realizations of the T-phase were computed in DFT and were very similar (-170 ± 2 meV/atom), consistent with the insensitivity of the T-phase to the precise Al/Zn occupations. We subsequently used the lowest energy structure (-171 meV/atom) for considering compositional changes. We note clearly that the T-phase formation energy is about 110 to 140 meV/atom lower than the formation energies of η'_{IV} and η'_I-phases, respectively, which is consistent with the observed stability of the T-phase. The fact that η' was observed at all might be attributed to its faster formation kinetics since η' requires less solutes (18 atoms) to build a single unit cell compared to T-phase (162 atoms).

We then examine the energetics of Cu substitution into the T-phase, i.e. replacing single Mg, Zn and Al atoms with a Cu atom. Due to the range of atomic sites and the randomness of the Al/Zn occupation, we have studied Cu-substitution into five random sites for each of the three elements. The energies after substitution, without relaxation, are computed. While there are non-negligible differences among the substitutions of Cu into the five random sites (range of ~300 meV), the trends are very clear. It is energetically unfavorable (energy change +781 to +1051 meV) to substitute Cu for Mg, it is quite favorable (energy change -89 to -396 meV) to substitute Cu for Al, and it is often, but not always, energetically favorable (energy change -156 to $+124$ meV) to substitute Cu for Zn. To examine the role of relaxations, we fully relaxed that structure having the lowest energy among all five substitutions for each case, as shown in Fig. 9. Relaxation reduces the energies by 75-300 meV, further stabilizing the Cu-substitutions for both Al and Zn but with substitution for Mg remaining highly unfavorable. These results align with our experimental deductions that additions of Cu increase nucleation and stability of T-phase. In addition, our results indicate that Cu-substitutions for Al are most favorable, consistent with experimental results in Fig. 4 showing reduced Al content in the T-phase when Cu is present.

We also note that the compositions of the T-precipitates observed in our experiments deviate from the equilibrium composition and can vary as a function of the processing applied. In general, we find that the Al content tends to be increased relative to the equilibrium form. We do not believe the experimental deviations from equilibrium T-phase alters our conclusions as they tend to have an increased concentration of Al sites relative to equilibrium which, as we noted, is the most favorable site for Cu substitution. If anything, it is likely that the compositions experimentally observed in this study are even more likely to benefit from dilute Cu than the equilibrium form.

Overall, the DFT findings for few-atom clusters, η'-phases (as surrogates for early nucleation) and T-phase show that Cu additions do not penalize few-atom cluster formation, while then lowering substantially the formation energies of both η'-phases and the T-phase, with the largest effects found for the T-phase. This implies that Cu assists in nucleation of these phases, enhancing both the kinetics of the nucleation and the density of precipitates, consistent with the trends observed in our experiments.

4. Discussion

The major experimental findings can be summarized as follows.

- After pre-aging (PA) both alloys offer beneficial mechanical properties including high uniform elongation and increased work hardening compared to the EN AW-5182 alloy (Fig. 1, Fig. 2). Distorted globular GPI-Zones are found in both alloys but are present at higher density and larger size in 5182-ZnCu (Table 5) with enhanced Cu-incorporation (Figs. 4 and 6a), which corresponds to the higher yield strength observed.
- Applying a paint bake treatment without pre-deformation (TMT 1) on 5182-Zn shows only a slight increase in yield strength (47 MPa) while 5182-ZnCu exhibits a sole paint bake response (sPBR) of 127 MPa (Table 3). T-phase reflection spots are evident in DPs of both alloys (Figs. 5b and 6b), but for 5182-ZnCu precipitates are smaller, less elongated and present at greater than five times higher number density (Table 5) and their chemical composition has already developed more towards the equilibrium condition, with Cu being incorporated into precipitates to some extent (Fig. 4).
- If 2% pre-deformation is applied before the paint bake treatment (TMT 2) 5182-Zn exhibits a giant hardening response of 178 MPa. The yield strength increase for 5182-ZnCu is even higher (184 MPa), but the effect of pre-strain is more pronounced for 5182-Zn than for 5182-ZnCu (Table 3). In 5182-Zn the hardening phase is smaller, less elongated, present at greater than three times higher number density compared to TMT 1 (Table 5), and additional reflection spots, which possibly correspond to precursors with η'-phase or η'-phase-like structures, can be found (Fig. 5c). Slight pre-straining led to an enhanced chemical development of precipitates towards equilibrium condition in both alloys but is more pronounced if Cu is present (5182-ZnCu). Additionally, the level of Cu-incorporation in precipitates is higher in TMT 2 condition (Fig. 4).
- DFT calculations performed show that Cu neither promotes nor hinders the formation of earliest stage solute pairs or triplets (Fig. 7) but stabilizes η'-precipitates (Fig. 8) and, to an even larger extent, T-precipitates (Fig. 9).

We now discuss these experimental results in detail.

4.1. Effect of alloy composition on the hardening behavior

Thermodynamic calculations [78,84] have shown that T-phase ($Mg_{32}(Al,Zn)_{49}$) or its precursors are the dominant hardening phases in the alloys investigated in this study, which was confirmed by the extra reflection spots at the 2/5 and 3/5 $\langle 022 \rangle$ Al position in the DPs after paint bake treatment (Fig. 5b and c, Fig. 6b and c). Hou et al. [49,51] recently conducted intensive TEM and APT work on a similar alloy and proposed the precipitation sequence to follow *SSSS (supersaturated solid solution) ➔ GPI zone (fully coherent) ➔ GPII zone (T", fully coherent) ➔ intermediate T' (semi-coherent) ➔ equilibrium T (incoherent)*, which will be used to discuss our findings.

After pre-aging (PA) TEM and APT analysis revealed the existence of dark spots/clusters without distinct crystal structure in both alloy, which were identified as GPI-zones. If Cu is present in the alloy the number density of GPI-zones is higher, their size is larger (Table 5) and Cu-incorporations are evident (Fig. 4) which is consistent with the higher strength observed (Fig. 1).

The absence of any strengthening effect of 5182-Zn after pre-aging is in contrast to some findings in literature [35,43,49] but can be explained by the significantly shorter pre-aging time applied in the current study and the total absences of Cu in the investigated 5182-Zn resulting in the observed lower number and smaller size of GPI-zones (Table 5) similarly found in earlier work by some of the present authors on a similar alloy [34].

Generally, GP-zones evolve from initially small solute clusters during a low temperature pre-aging treatment [35,43,49,51]. The boosting effect of Cu on GP-zone formation and growth in Mg-containing alloys and the resulting enhanced strengthening (similarly observed in this study, Fig. 1c) is well reported in aluminum alloys corresponding to the 2xxx-series [85–88], 6xxx-series [54,89–91] and 7xxx-series [92–94] with low Mg/Zn ratio. In Cu-containing 5xxx-series alloys (AlMgCu) [21,23–25,95] and 2xxx-series alloys(AlCuMg) this effect has been linked to Mg-Cu-cluster hardening, the earliest stage of S-Al_2MgCu precipitation, which was also suggested for Zn- and Cu-containing 5xxx-series alloys (AlMgZnCu) with high Mg/Zn ratio [48,49] but detailed information is limited due to the novelty of such alloys and the mechanisms behind are still not fully understood as it seems to be strongly dependent on alloy composition and the heat treatment applied [43,49–52].

However, according to the APT analysis conducted GPI-zones in 5182-ZnCu incorporate 0.6 at.% Cu after low-temperature pre-aging (Fig. 4), three times as much as in the surrounding matrix (Table 4). Similar results were also reported by Cao et al. [43], which additionally supports the early-stage effect of Cu. It was recently proposed by Geng et al. [35] that Cu incorporation in early-stage Mg-Zn clusters might reduce the strain energy resulting from the differences in atomic radii of Mg and Zn. As a consequence, these strain-relieved clusters are supposed to be less effective trapping sites for vacancies, making them available for enhanced solute diffusion boosting their growth. Even though this proposal accounts well for a larger size of GPI-zones observed it does not explain the increased number density observed. The reported low total Cu content (similar to the investigated 5182-ZnCu) and its limited diffusion rate at low temperatures [96,97] compared to Zn and Mg might suggest that Cu affects the initial stage of precipitate formation rather than later stages of aging.

According to our DFT calculations Cu does not help nor significantly hinder the formation of earliest-stage clusters on the smallest scale (pairs/triplets). Individual Cu atoms are thus incorporated into these initial solute clusters at random. With increasing cluster size (more than three atoms) the number of possible cluster configurations already becomes unmanageable, so we assume η' (consisting of 18 atoms per unit cell) as a surrogate representation for a transient phase (described and discussed in Section 3.3 for easier readability) to access the next larger length scale by DFT. The addition/incorporation of Cu atoms at low concentrations (well-separated in the cluster) was found to stabilize the clusters (see Fig. 8). Additionally, the incorporation of Cu did not hinder in any way a further increase in either Mg or Zn solute content (by replacing Al atoms) revealing a Mg/(Zn+Cu) ratio of 0.71 for the most beneficial η'-configuration $Mg_4(Zn_5Cu)(Al_6ZnMg)$. This finding correlates well with the average Mg/(Zn+Cu) ratio of 0.70 found for GPI-zones in 5182-ZnCu after pre-aging (PA) and might support the assumption that η'-surrogate clusters indeed act as early-stage transition phase in the development of the T-phase. Since the Cu atoms stabilize such clusters, more clusters can nucleate (preferentially around Cu atoms) thus finally resulting in an increased number density of GPI-zones as observed (Table 5).

After paint bake treatment without pre-deformation (TMT 1) on 5182-Zn large elongated precipitates in low number density (0.3×10^{23} m^{-3}, Table 5) are present in the matrix (Fig. 5b) and accountable for the strength increase of 47 MPa. In contrast, the same treatment results in an almost five times higher number density (1.6×10^{23} m^{-3}) of smaller and more globular (Table 5 and Fig. 16 in the Appendix) precipitates and a significantly higher hardening response of 127 MPa in 5182-ZnCu (Fig. 6b). Extra reflection spots in the DPs indicated that GPI-zones found after pre-aging (PA) have evolved into precipitates with a distinct T-phase crystal structure. Based on the APT results these precipitates have grown during the paint bake treatment by enhanced diffusion of Mg and Zn and have developed a chemical composition close to that of the reported T' [28] but did not reach the equilibrium composition of the T-phase yet (Fig. 4) which identifies them as precursors of T-phase (intermediate T') [35,48,51]. In 5182-ZnCu the precipitate composition is already more developed and closer to equilibrium condition (Fig. 4), clearly identifying them as T'-phase. Their significant enrichment with Cu (0.6 at.%) additionally suggests an increased hardenability [52,92].

The hardening precipitates observed after both TMT 1 and TMT 2 are assumed to develop from or nucleate at stable GPI-zones present after pre-aging by enhanced solute diffusion and incorporation during the high-temperature paint bake treatment which is in agreement with the generally accepted nucleation and growth theory [20,98]. Earlier work by some of the present authors additionally supports this as no reduction of hardness (no dissolution of precursors, which contribute to strengthening) was observed in the early stages of the 2nd stage aging [34].

To discuss the development of hardening phases during the 2nd aging stage in detail, we first consider only the effect of size. Based on APT data the number and size distribution of GPI-zones after pre-aging is significantly affected by the presence of Cu (as shown in Fig. 10a).

Comparing the number of GPI-zones after PA and the number of precipitates after TMT 1 (Table 5) reveals that less than 10% of GPI-zones have evolved into large, elongated intermediate T' in 5182-Zn while more than 30% developed into small, mostly globular precipitates in 5182-ZnCu (Fig. 16 in the Appendix), which is consistent with different strength increments observed (Table 3). Under the assumption that only the largest GPI-zones were stable enough for growth and development during the 2nd aging stage [20,98], we observe that only GPI-zones exceeding a size of roughly 700 atoms (indicated by the dashed blue line in Fig. 10a) have developed into T-precursors in the investigated alloys. This suggests that Cu-additions not only support nucleation of GPI-zones (as mentioned above) but also facilitate their growth and subsequent development, which is consistent with results found by Chinh et al. [93] and Deschamps et al. [92] in Cu-containing AlZnMg alloys.

In terms of chemical development, the evolution of T-phase is supposed to proceed in a gradual manner (as observed in Fig. 4) and precursors with significantly deviating crystal structure from equilibrium condition have not been reported in similar alloys yet. The presence of fainted reflection spots corresponding to η'- or η'-like precipitates found in 5182-Zn after TMT 2 (see DP in Fig. 5c) is in contrast to reported results [35,43,49] and might indicate that such precipitates could act as surrogate transition phase in the development of T-phase as already mentioned above.

For AlZnMg(Cu) alloys, whose precipitation sequence follows SSSS ➔ GP-zone ➔ intermediate η' ➔ equilibrium η, both GP-zones and η' are reported to exhibit a Mg/(Zn+Cu) ratio of 0.7 to 1.0 [82], which matches well with our results revealing that GPI-zones exceeding the size of roughly 700 atoms in both alloys additionally exhibit Mg/(Zn+Cu) ratios higher than 0.7 (see Fig. 10b and Fig. 10c). According to Hou et al. [51] the development of GPI-zones is easier if their chemical composition is closer to that of
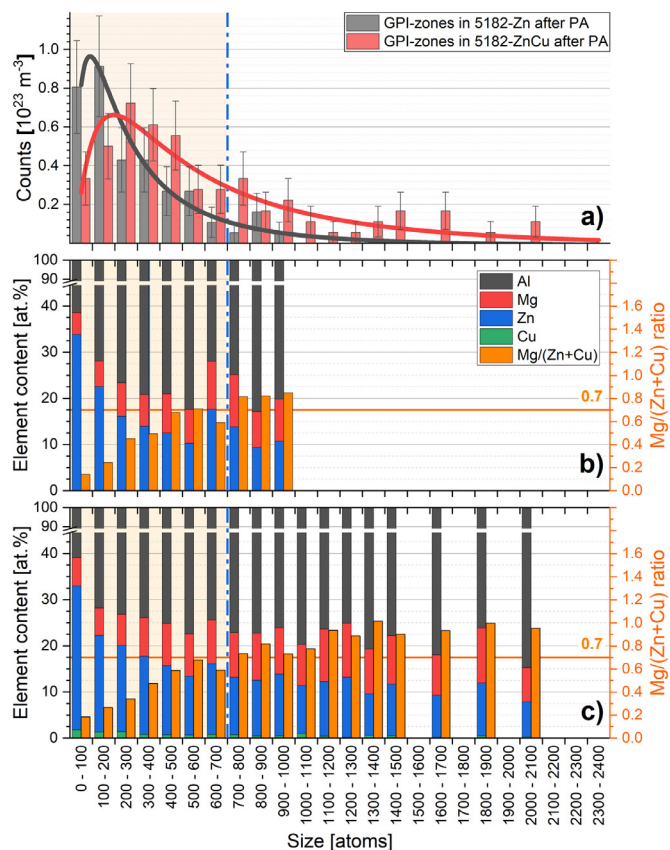

Fig. 10. Size distribution of GPI-zones in 5182-Zn (black) and 5182-ZnCu (red) after pre-aging (PA) based on APT data (a), GPI-zone composition for each size class of 5182-Zn (b) and 5182-ZnCu (c). The legend shown in b is the same for c. GPI-zones, which exceed a size of roughly 700 atoms (indicated by dashed blue vertical lines) and exhibit a higher Mg/(Zn+Cu) ratio than 0.7 (indicated by the full orange horizontal line in b and c) tend to develop into precipitates upon subsequent thermomechanical treatment. (For interpretation of the references to color in this figure, the reader is referred to the web version of this article.)

the next evolution stage suggesting a more likely evolution of GPI-zones into transient η'-surrogates before subsequent development into T' instead of a direct transformation into T', whose Mg/(Zn+Cu) ratio is much higher (~1.4). If Cu is present the evolution sequence proposed is therefore assumed to be additionally facilitated due to the stabilizing effect of Cu-substitution on η'-surrogates revealed by our DFT calculations (Fig. 8).

Due to the fact that η' reflection spots are very fainted in 5182-Zn (indicating an only minor phase fraction) and absolutely absent 5182-ZnCu it is assumed that the subsequent development of transient η' into T'/T is energetically even more favorable than remaining a η'-structure, regardless of the Cu-content. According to our DFT calculations the development into T-phase structure (which is similar to that of intermediate T' [28]) is indeed more beneficial, revealing an average energetic benefit of approximately 110 and 140 meV/atom compared to η'$_{IV}$- and η'$_{I}$-phase, respectively. If Cu is present and substituted into Al or Zn-lattice sites of the T-phase, its stability is even more enhanced (Fig. 9) resulting in an even higher driving force for phase transformation, which explains why η' was not observed at all in 5182-ZnCu (Fig. 6b and c) and is also consistent with the trends in precipitate composition observed (Fig. 4).

4.2. Effect of alloy composition on the forming performance

Additional to the beneficial hardening of the investigated alloys, promising results were also found regarding their forming perfor-

mance. In their dedicated forming condition (after PA) the elongation of both investigated alloys is not deteriorated (even though both alloys show a different yield strength) and their work hardening ability is increased compared to the EN AW-5182 (Fig. 2a). The observed shift to higher strain hardening rates (SHR) and their inhibited decrease to lower levels (Fig. 2b) can be linked to enhanced dislocation formation and inhibited dislocation annihilation during deformation [34,75–77], which might be attributed to dynamic precipitation during deformation as proposed by Deschamps et al. [99]. Due to the only short-term pre-aging applied in this study the supersaturation of solutes remains on a high level (Table 4), which is assumed to decrease by dynamic precipitation during the deformation process resulting either in dynamic growth of pre-existing GPI-zones or nucleation of new precipitates in the matrix. In both cases dynamic recovery is inhibited, and the work hardening remains on a high level. Additionally, the precipitation process might limit the interaction of Mg with dislocations during deformation to some extent [36] and might therefore contribute to the observed delayed onset of serrated flow.

4.3. Effect of pre-straining on the hardening behavior

If 2 % pre-strain is applied after pre-aging and before the final paint bake treatment (TMT 2) the THR reaches 178 MPa in 5182-Zn and 184 MPa in 5182-ZnCu. If corrected to the strength contribution of hardening precipitates only, the sPBR is 134 MPa and 147 MPa, respectively. This corresponds to a benefit of 87 MPa (5182-Zn) and 20 MPa (5182-ZnCu) over TMT 1 and results in final yield strengths of 353 MPa and 410 MPa, respectively. The boosting effect of 2% pre-strain on the hardening response in 5182-Zn is even more remarkable if compared to a commercial EN AW-6016 (pre-aged for 5h at 100°C) for which the benefit of 5% pre-strain is only ~30 MPa in total yield strength [100].

Generally, the beneficial effect of pre-straining on the hardening response is reported in several Al-alloys and has been shown to be strongly related to dislocations introduced by deformation. In contrast to the most published work, which reports pre-deformation prior to pre-aging to suppress natural aging by vacancy annihilation [7,53,54], detailed information on the positive effect of pre-strain after pre-aging is limited.

To account for the pre-deformation applied in the current study, we first need to consider the effect of the introduced dislocations and their evolution upon paint bake treatment. It can be seen from Fig. 1 and Table 3 that 2% pre-straining results in dislocation hardening of approximately 60 MPa. This yield stress contribution can be estimated by the Taylor hardening model as [101]:

$$\sigma = \alpha \cdot b \cdot G \cdot M \sqrt{\rho} \tag{1}$$

with α as constant (0.3), b Burgers vector (0.286 nm), G shear modulus (25.4 GPa), M Taylor factor (3.06) and ρ dislocation density. Therefore, the observed strengthening effect (53 MPa) in EN AW-5182 corresponds to an estimated increase in dislocation density of about 6.6×10^{13} m^{-2}.

Upon paint bake treatment (185°C/20 min) of EN AW-5182 a strength loss of 24 MPa (Table 3) is observed, which corresponds to a reduction in dislocation density of about 4.6×10^{13} m^{-2}. The dislocations, which are homogeneously distributed in the state before the paint bake treatment (similarly observed for the investigated alloys and shown in Fig. 11) thus travel through the crystal, rearrange and partly annihilate. Comparable observations on recovery, i.e. reduction of dislocation density during a paint bake treatment, were also made by Gruber et al. [100] on a pre-aged and pre-strained (10%) EN AW-6016 (AlMgSi) via synchrotron experiments and are in good agreement with our estimations.

It is reasonable to assume that recovery processes observed in EN AW-5182 also occur in both investigated alloys (although prob-
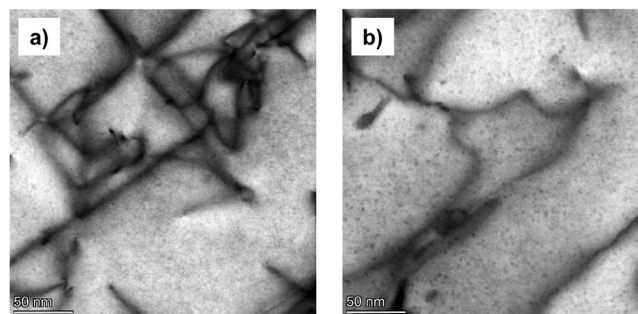

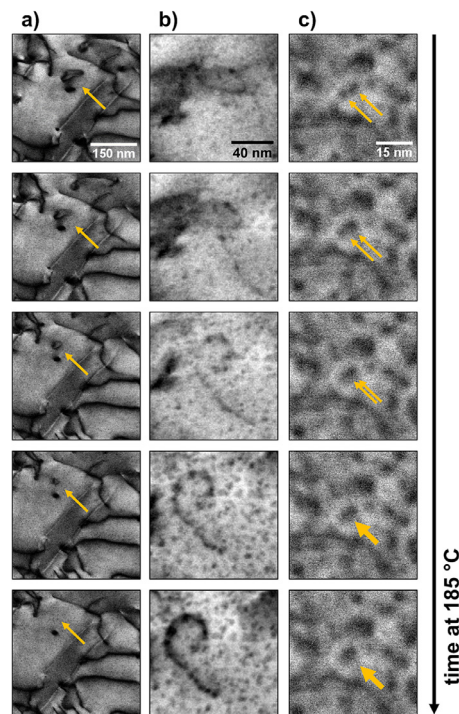**Fig. 11.** BF-TEM images of 5182-Zn (a) and 5182-ZnCu (b) in PS condition.

Fig. 12. Evolution of microstructural features in pre-aged and pre-deformed 5182-ZnCu during *in-situ* STEM heat treatment acquired by BF-STEM detector. Dislocation annihilation (a), Dislocation-assisted growth of precipitates (b), Coalescence of growing precipitates (c). Note that image sequences were acquired at different aging times and at varying time steps for better visualization. Scale bars shown in the first images (top) corresponds to the whole sequence. Experimental details are provided in section 2.

ably to a smaller extent due to reduced kinetics caused by the presence of GPI-zones [99]). Dislocation annihilation was indeed observed during *in-situ* STEM heat treatments on pre-strained (PS) samples of both alloys and is shown for 5182-ZnCu in Fig. 12a as an example (for experimental details the reader is referred to Section 2). At paint bake temperature (185°C), dislocations start to travel through the matrix. While some dislocations rearrange and annihilate, others are pinned by larger GPI-zones (Fig. 12b) throughout the heat treatment, which limits recovery to some extent.

Now we discuss the effect of dislocations on the hardening precipitates. As experimentally observed (Fig. 12b), pinned dislocations can act as sinks for segregated solutes resulting in preferential nucleation sites for new precipitates. Additionally, too small and thus unstable GPI-zones might be stabilized by the reduction of their total strain energy leading to a decrease in critical size

for subsequent growth [20,98]. In both cases dislocation-assisted pipe diffusion [102–104] accelerates solute transport resulting in enhanced growth and chemical evolution of GPI-zones into T'-precipitates as observed by TEM and APT analysis. The comparison of the solute content after TMT 1 and TMT 2 (i.e. without and with pre-straining, see Table 4) provides an additional indication for enhanced solute consumption by precipitates.

To understand the different effect of pre-deformation on the two alloys investigated here, we need to have a closer look at the initial conditions before paint bake. Based on the size distribution of GPI-zones after pre-aging (Fig. 10a) we know that in the Cu-free alloy 5182-Zn a significantly smaller amount of large-sized GPI-zones is present compared to the Cu-containing alloy 5182-ZnCu.

If no pre-deformation is applied, no or just a few dislocations are available to act as sinks for segregated solutes during paint bake treatment. Supersaturated solutes and dissolving GPI-zones contribute to the extensive growth of the few larger and, therefore, stable GPI-zones, which finally results in a low number density (compared to PA condition, see Table 5) of elongated hardening phase and an only minor strength gain. In 5182-ZnCu small GPI-zones also dissolve but, in contrast, the significantly higher number of larger GPI-zones, which are able to grow and develop into mostly globular T'-precipitates, inhibits a drastic decrease in number density, as observed in 5182-Zn, to some extent and finally results in a significantly larger strength increase compared to the Cu-free alloy (Table 3).

If pre-deformation is applied on 5182-Zn, the unrecovered dislocations boost nucleation of precipitates and assist the development of pre-existing GPI-zones (as mentioned above). As a consequence, the extensive growth and decline in number density observed during the paint bake of non-deformed 5182-Zn is prevented resulting in a three times higher number density of precipitates (see Table 5) and a significant strength increase of 178 MPa after TMT 2.

For pre-deformed 5182-ZnCu the same mechanisms apply but in contrast to the Cu-free alloy dislocation annihilation is slightly more inhibited during the paint bake treatment due to the increased pinning force resulting from the higher number of larger GPI-zones already present after pre-aging (Fig. 10 and Fig. 16b in the Appendix). The dense network of pinned dislocations and the smaller average distance between GPI-zones thus lead to an additional phenomenon observed during the *in-situ* STEM heat treatment. With dislocation-enhanced growth and development into precipitates, some closely adjacent precipitates were found to undergo a solid-state coalescence/agglomeration (shown in Fig. 12c), thereby decreasing their interfacial energy [20,105]. Although defective identification and counting of closely adjacent precipitates by cluster search cannot be fully precluded, coalescence of precipitates can explain the wide variation of morphology observed (Fig. 16f) and is also consistent with the lower number density of T'-precipitates found after TMT 2 (Table 5). Interestingly, the chemical development of these precipitates is significantly more advanced (Fig. 4) compared to 5182-ZnCu in TMT 1 condition. As a consequence, the hardenability of these precipitates is assumed to be similar or higher due to their increased Cu content [52,92] and can explain the higher strength gain of 184 MPa after TMT 2. In addition, the limited dislocation annihilation might also contribute to the higher strength observed.

5. Conclusion

In this study a new thermomechanical treatment was applied on two AlMgZn(Cu) alloys based on commercial EN AW-5182 and modified with additions of Zn (5182-Zn) and Zn+Cu (5182-ZnCu),

to improve their industrial application potential for future automotive sheets.

After short-term pre-aging (100 °C/3 hours) both alloys reveal an advanced forming performance by offering increased work hardenability without the elongation being deteriorated compared to their commercial EN AW-5182 base alloy. These beneficial effects are associated with the fine-scale distribution in homogeneously dispersed GPI-zones resulting from the preceded short-term low temperature pre-aging treatment introduced. If Cu is present (5182-ZnCu) a slightly higher yield strength is obtained after pre-aging resulting from a higher number density of larger Cu-incorporated GPI-zones. The beneficial effect of Cu on precipitate formation and growth was additionally confirmed by intensive DFT calculations revealing a significant decrease of energy in the presence of Cu.

Applying a paint bake treatment (20 min short heat treatment at 185°C) on the pre-aged and non-deformed alloy sheets the yield strength of 5182-Zn increased by 47 MPa while 5182-ZnCu showed a strong hardening response of 127 MPa revealing a yield strength of 353 MPa and therefore already significantly exceeding the strength of most AlMgSi alloys after similar heat treatment. Hardening precipitates identified as precursors of T-phase (intermediate T') have evolved from stable GPI-zones formed during pre-aging and exist at a higher number density and higher degree of chemical evolution in the Cu-containing alloy 5182-ZnCu, resulting in the higher yield strength observed. The beneficial effect of Cu can be explained by its stabilizing effect enhancing both nucleation and growth of T-phase and its precursors over the whole precipitation sequence.

By performing a pre-deformation of 2% after pre-aging the hardening response during paint bake treatment is additionally boosted. The reported giant strength increase of 178 MPa and 184 MPa in 5182-Zn and 5182-ZnCu, respectively, exceeds any reported hardening response during a paint bake treatment so far. Also, they still sustain adequate elongation and work hardenability regardless their remarkable yield strengths of 335 MPa (5182-Zn) and 410 MPa (5182-ZnCu). The applied pre-straining enhances the chemical development of precipitates in both alloys by dislocation-assisted solute transport, promotes Cu enrichment in case of 5182-ZnCu and strongly increases the number density of hardening precipitates in 5182-Zn. The latter effect is attributed to the introduction of new nucleation sites and the stabilization of pre-existing ones by dislocations facilitating precipitate development.

In our study we have shown that applying our thermomechanical treatment on AlMgZn(Cu) alloys results in a beneficial mechanical performance in both soft and especially in hard temper to adequately addresses the long-standing trade-off between high strength and good formability and achieve a satisfactory balance. Additionally, our proposed treatment strategy can cope with industrial processing requirements and exploit the alloys' full potential for automotive sheet production. Their wide application represents a way to establish a single-alloy concept for sheet material (but not necessarily limited to) and thus contributes to a sustainable improvement in the recyclability of future automotive vehicles.

Data availability

The raw/processed data required to reproduce these findings cannot be shared at this time as the data also forms part of an ongoing study.

Declaration of Competing Interest

The authors declare that they have no known competing financial interests or personal relationships that could have appeared to influence the work reported in this paper.

CRediT authorship contribution statement

Lukas Stemper: Conceptualization, Methodology, Investigation, Visualization, Writing - original draft. **Matheus A. Tunes:** Investigation, Visualization, Writing - review & editing. **Phillip Dumitraschkewitz:** Investigation, Writing - review & editing. **Francisca Mendez-Martin:** Investigation, Writing - review & editing. **Ramona Tosone:** Writing - review & editing. **Daniel Marchand:** Investigation, Writing - review & editing. **William A. Curtin:** Investigation, Writing - review & editing. **Peter J. Uggowitzer:** Conceptualization, Supervision, Writing - review & editing. **Stefan Pogatscher:** Project administration, Conceptualization, Supervision, Writing - review & editing.

Acknowledgements

Supplementary materials

Supplementary material associated with this article can be found, in the online version, at doi:10.1016/j.actamat.2020.116617.
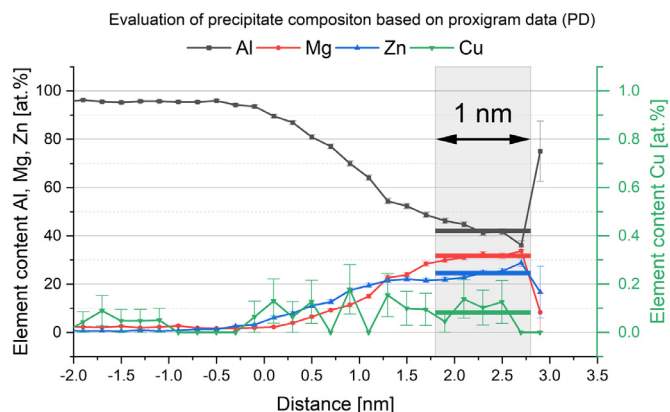

Fig. 13. Evaluation of precipitate composition based on proxigram data (PD). Grey array corresponds to values taken into account for composition. Thick colored lines indicate the average element content of corresponding element. (For interpretation of the references to color in this figure, the reader is referred to the web version of this article.)

APPENDIX

Error estimation for number densities evaluated from APT data

The number density (n) is defined by the number of detected features (N) within an analyzed volume (V), which corresponds to the volume measured (V_m) by enveloping the analyzed region in a convex hull utilizing the built-in function "AlphaShape" in MATLAB[TM] [64], and is calculated by

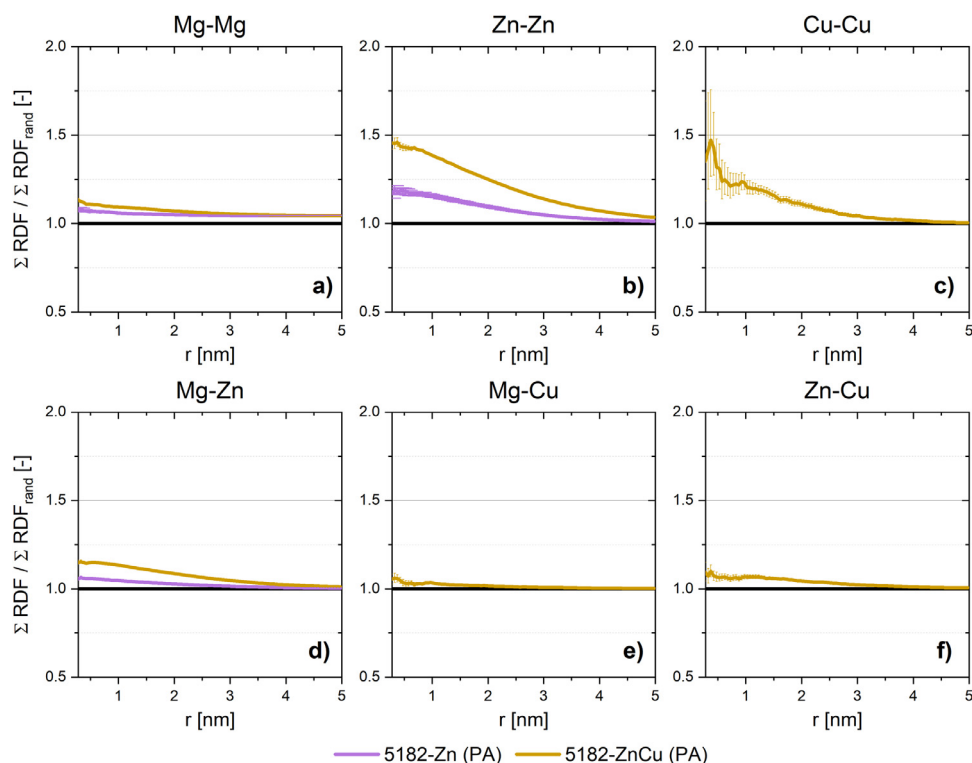$$n = \frac{N}{V} \tag{2}$$

$$V = V_m \tag{3}$$

Fig. 14. Plots of normalized radial distribution functions (RDF) for Mg-Mg (a), Zn-Zn (b), Cu-Cu (c), Mg-Zn (d), Mg-Cu (e) and Zn-Cu (f) after pre-aging (PA) of both alloys. Values > 1 indicate non-random distribution (clustering).
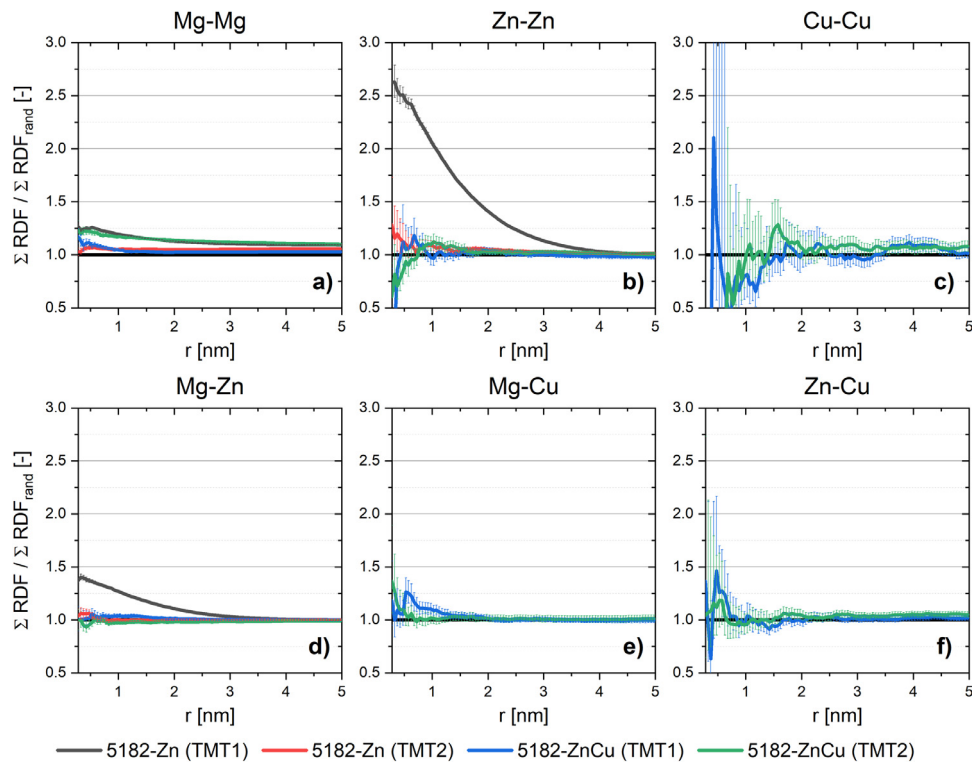
Fig. 15. Plots of normalized radial distribution functions (RDF) for Mg-Mg (a), Zn-Zn (b), Cu-Cu (c), Mg-Zn (d), Mg-Cu (e) and Zn-Cu (f) after TMT 1 and TMT 2 of both alloys. Values > 1 indicate non-random distribution (clustering).

Assuming a Poisson distribution of features within an analyzed volume [65] allows to estimate the sampling error resulting from miscounting (s_N) by

$$s_N = \sqrt{N} \tag{4}$$

The error in number density resulting from volume analysis (s_V) is determined by

$$s_V = V_m - V_{theor} = V_m * \left(1 - \frac{V_{th}}{V_m}\right) = V * \left(1 - \frac{V_{th}}{V}\right) \tag{5}$$

with V_{th} as the theoretical volume of the analyzed volume determined from the corresponding total number of detected atoms (N_{atoms}) and its ideal atomic density, calculated by

$$V_{th} = N_{atoms} * \frac{m * \eta}{a^3} \tag{6}$$

where m is the number of atoms within an fcc-Al unit cell (4), η is the detecting efficieny (0.37) and a is the lattice constant of aluminum (0.405).

The total estimated error in number density (s_{tot}) is then derived from the Gaussian law of error propagation as

$$s_{tot} = \sqrt{\left(\frac{\partial n}{\partial N} * s_N\right)^2 + \left(\frac{\partial n}{\partial V} * s_V\right)^2} \tag{7}$$

$$s_{tot} = \sqrt{\frac{N}{V^2} + \frac{N^2}{V^2} * \left(1 - \frac{V_{th}}{V}\right)^2} \tag{8}$$
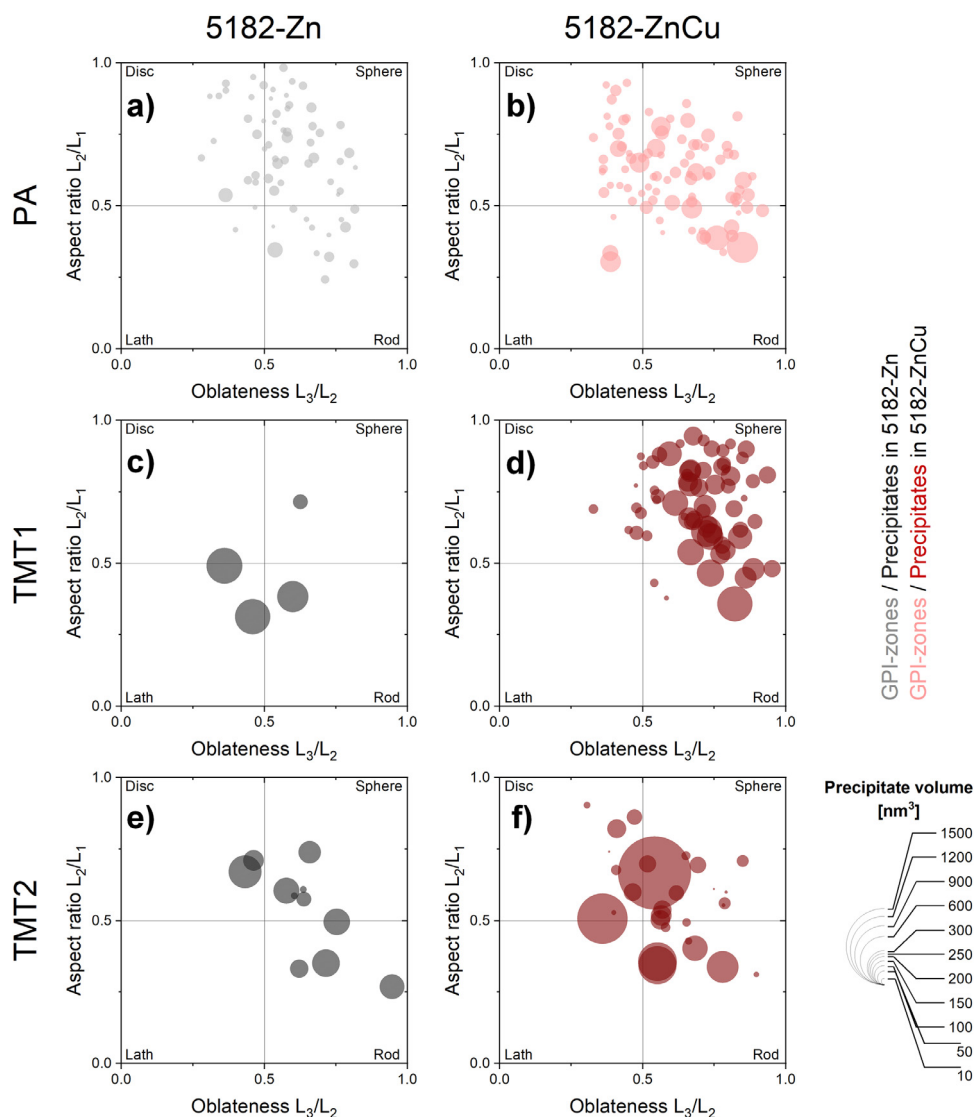
Fig. 16. Morphology distribution of GPI-zones and precipitates for each alloy and condition. The area of the circles indicates the ellipsoid volume of each precipitate detected in the corresponding APT data set. For details see section 2.

References

[1] J. Hirsch, Recent development in aluminium for automotive applications, Trans. Nonferrous Metals Soc. China 24 (2014) 1995–2002.

[2] J. Hirsch, Aluminium in innovative light-weight car design, Mater. Trans. 52 (2011) 818–824.

[3] D. Carle, G. Blount, The suitability of aluminium as an alternative material for car bodies, Mat. Des. 20 (1999) 267–272.

[4] Cui Jirang, H.J. Roven, Recycling of automotive aluminum, Trans. Nonferrous Metals Soc. China 20 (2010) 2057–2063.

[5] D. Raabe, C.C. Tasan, E.A. Olivetti, Strategies for improving the sustainability of structural metals, Nature 575 (2019) 64–74.

[6] S.K. Das, J.A.S. Green, J.G. Kaufman, The development of recycle-friendly automotive aluminum alloys, JOM 59 (2007) 47–51.

[7] Y. Birol, Pre-straining to improve the bake hardening response of a twin-roll cast Al–Mg–Si alloy, Scr. Mater. 52 (2005) 169–173.

[8] S. Hirth, G. Marshall, S. Court, D. Lloyd, Effects of Si on the aging behaviour and formability of aluminium alloys based on AA6016, Mater. Sci. Eng., A 319-321 (2001) 452–456.

[9] M.X. Guo, G. Sha, L.Y. Cao, W.Q. Liu, J.S. Zhang, L.Z. Zhuang, Enhanced bake-hardening response of an Al–Mg–Si–Cu alloy with Zn addition, Mater. Chem. Phys. 162 (2015) 15–19.

[10] L. Yan, Z. Li, Y. Zhang, B. Xiong, X. Li, H. Liu, S. Huang, et al., Pre-aging on early-age behavior and bake hardening response of an Al-0.90Mg-0.80Si-0.64Zn-0.23Cu alloy, Prog. Nat. Sci. 26 (2016) 398–403.

[11] F. Ostermann, Anwendungstechnologie Aluminium, Springer Berlin Heidelberg, Berlin/Heidelberg, 2014.

[12] E.L. Huskins, B. Cao, K.T. Ramesh, Strengthening mechanisms in an Al–Mg alloy, Mater. Sci. Eng., A 527 (2010) 1292–1298.

[13] W. Sylwestrowicz, E.O. Hall, The deformation and ageing of mild steel, Proc. Phys. Soc. London Sect. B 64 (1951) 495.

[14] A. Portevin, F.Le Chatelier, Sur un phénomène observé lors de l'essai de traction d'alliages en cours de transformation, Comptes Rendus de l'Académie des Sciences Paris 176 (1923) 507–510.

[15] H.-P. Falkenstein, W. Gruhl, in: Forming Behavior of Aluminum, 19, Bander-Bleche- Rohre, 1978, pp. 265–268.

[16] R.E. Sanders, S.F. Baumann, H.C. Stumpf, Non-heat-treatable aluminum alloys, Alum. Alloys 3 (1986) 1441–1484.

[17] A.H. Naronikar, H.A. Jamadagni, A. Simha, B. Saikiran, Optimizing the heat treatment parameters of Al-6061 required for better formability, Mater. Today 5 (2018) 24240–24247.

[18] H. Zhong, P.A. Rometsch, X. Wu, L. Cao, Y. Estrin, Influence of pre-ageing on the stretch formability of Al-Mg-Si automotive sheet alloys, Mater. Sci. Eng., A 697 (2017) 79–85.

[19] H. Zhong, P.A. Rometsch, L. Cao, Y. Estrin, The influence of Mg/Si ratio and Cu content on the stretch formability of 6xxx aluminium alloys, Mater. Sci. Eng., A 651 (2016) 688–697.

[20] D.A. Porter, K.E. Easterling, M.Y. Sherif, Phase Transformations in Metals and Alloys, CRC Press, Boca Raton, FL, 2009.

[21] O. Engler, C.D. Marioara, T. Hentschel, H.-J. Brinkman, Influence of copper additions on materials properties and corrosion behaviour of Al–Mg alloy sheet, J. Alloys Compd. 710 (2017) 650–662.

[22] M. Hino, S. Koga, S. Oie, M. Yanagawa, Properties of Al-Mg based alloys for automobile body panel, Kobelco Technol. Rev. (1991).

[23] A. Alil, M. Popović, T. Radetić, M. Zrilić, E. Romhanji, Influence of annealing temperature on the baking response and corrosion properties of an Al–4.6wt% Mg alloy with 0.54wt% Cu, J. Alloys Compd. 625 (2015) 76–84.

[24] P. Ratchev, B. Verlinden, P. de Smet, P. van Houtte, Artificial ageing of Al–Mg–Cu alloys, Mater. Trans. (1999) 34–41.

[25] P. Ratchev, B. Verlinden, P. de Smet, P. van Houtte, Precipitation hardening of an Al–4.2wt% Mg–0.6wt% Cu alloy, Acta Mater. (1998) 3523–3533.

[26] L. Kovarik, M.K. Miller, S.A. Court, M.J. Mills, Origin of the modified orientation relationship for S(S″)-phase in Al–Mg–Cu alloys, Acta Mater. 54 (2006) 1731–1740.

[27] A. Charai, T. Walther, C. Alfonso, A.-M. Zahra, C.Y. Zahra, Coexistence of clusters, GPB zones, S″-, S′- and S-phases in an Al–0.9% Cu–1.4% Mg alloy, Acta Mater. 48 (2000) 2751–2764.

[28] A. Bigot, P. Auger, S. Chambreland, D. Blavette, A. Reeves, Atomic scale imaging and analysis of T′ precipitates in Al-Mg-Zn alloys, Microsc. Microanal. Microstruct. 8 (1997) 103–113.

[29] G. Bergman, J.L.T. Waugh, L. Pauling, The crystal structure of the metallic phase Mg32(Al, Zn)49, Acta Cryst. 10 (1957) 254–259.

[30] C. Meng, Di Zhang, H. Cui, L. Zhuang, J. Zhang, Mechanical properties, intergranular corrosion behavior and microstructure of Zn modified Al–Mg alloys, J. Alloys Compd. 617 (2014) 925–932.

[31] K. Matsumoto, Y. Aruga, H. Tsuneishi, H. Iwai, M. Mizuno, H. Araki, Effects of Zn addition and aging condition on serrated flow in Al-Mg alloys, Mater. Sci. Forum 794-796 (2014) 483–488.

[32] J. Yun, S. Kang, S. Lee, D. Bae, Development of heat-treatable Al-5Mg alloy sheets with the addition of Zn, Mater. Sci. Eng., A 744 (2019) 21–27.

[33] X.B. Yang, J.H. Chen, J.Z. Liu, F. Qin, J. Xie, C.L. Wu, A high-strength AlZnMg alloy hardened by the T-phase precipitates, J. Alloys Compd. 610 (2014) 69–73.

[34] L. Stemper, M.A. Tunes, P. Oberhauser, P.J. Uggowitzer, S. Pogatscher, Age-hardening response of AlMgZn alloys with Cu and Ag additions, Acta Mater. 195 (2020) 541–554.

[35] Y. Geng, Di Zhang, J. Zhang, L. Zhuang, On the suppression of Lüders elongation in high-strength Cu/Zn modified 5xxx series aluminum alloy, J. Alloys Compd. (2020) 155-138.

[36] K. Matsumoto, Y. Aruga, H. Tsuneishi, H. Iwai, M. Mizuno, H. Araki, Effects of precipitation state on serrated flow in Al-Mg(-Zn) alloys, Mater. Trans. 57 (2016) 1101–1108.

[37] P. Ebenberger, P.J. Uggowitzer, S. Kirnstötter, B. Gerold, S. Zaefferer, S. Pogatscher, Processing-controlled suppression of Lüders elongation in AlMgMn alloys, Scr. Mater. 166 (2019) 64–67.

[38] P. Ebenberger, P.J. Uggowitzer, B. Gerold, S. Pogatscher, Effect of compositional and processing variations in new 5182-Type AlMgMn alloys on mechanical properties and deformation surface quality, Materials (Basel, Switzerland) (2019) 12.

[39] M. Carroll, P. Gouma, M. Mills, G. Daehn, B. Dunbar, Effects of Zn additions on the grain boundary precipitation and corrosion of Al-5083, Scr. Mater. 42 (2000) 335–340.

[40] C.-Y. Meng, Di Zhang, P.-P. Liu, L.-Z. Zhuang, J. Zhang, Microstructure characterization in a sensitized Al–Mg–Mn–Zn alloy, Rare Met. 37 (2015) 129–135.

[41] J. Zhao, B. Luo, K. He, Z. Bai, B. Li, W. Chen, Effects of minor Zn content on microstructure and corrosion properties of Al–Mg alloy, J. Cent. South Univ. 23 (2016) 3051–3059.

[42] P. Villars, K. Cenzual, Mg32(Al,Zn)49 (Mg32Zn31.9Al17.1) crystal structure: datasheet from "PAULING FILE Multinaries Edition, SpringerMaterials, *Springer-Verlag Berlin Heidelberg & Material Phases Data System (MPDS)*, Switzerland & National Institute for Materials Science (NIMS), Japan, 2012 materials.springer.com/isp/crystallographic/docs/sd_1252007.

[43] C. Cao, Di Zhang, L. Zhuang, J. Zhang, Improved age-hardening response and altered precipitation behavior of Al-5.2Mg-0.45Cu-2.0Zn (wt%) alloy with pre-aging treatment, J. Alloys Compd. 691 (2017) 40–43.

[44] N. Afify, A.-F. Gaber, G. Abbady, Fine scale precipitates in Al-Mg-Zn alloys after various aging temperatures, MSA 02 (2011) 427–434.

[45] H. Inoue, T. Sato, Y. Kojima, T. Takahashi, The temperature limit for GP zone formation in an Al-Zn-Mg alloy, Metall. Mat. Trans. A 12 (1981) 1429–1434.

[46] I.J. Polmear, Light Alloys: Metallurgy of the Light Metals, 3rd ed., Arnold, London, 1999.

[47] I.J. Polmear, D. StJohn, J.-F. Nie, M. Qian, Light Alloys: Metallurgy of the Light Metals, Butterworth-Heinemann, Oxford, 2017.

[48] C. Cao, Di Zhang, Z. He, L. Zhuang, J. Zhang, Enhanced and accelerated age hardening response of Al-5.2Mg-0.45Cu (wt%) alloy with Zn addition, Mater. Sci. Eng., A 666 (2016) 34–42.

[49] S. Hou, P. Liu, Di Zhang, J. Zhang, L. Zhuang, Precipitation hardening behavior and microstructure evolution of Al–5.1 Mg–0.15Cu alloy with 3.0Zn (wt%) addition, J. Mater. Sci. 53 (2018) 3846–3861.

[50] L. Stemper, B. Mitas, T. Kremmer, S. Otterbach, P.J. Uggowitzer, S. Pogatscher, Age-hardening of high pressure die casting AlMg alloys with Zn and combined Zn and Cu additions, Mater. Des. 181 (2019) 107927.

[51] S. Hou, Di Zhang, Q. Ding, J. Zhang, L. Zhuang, Solute clustering and precipitation of Al-5.1Mg-0.15Cu-xZn alloy, Mater. Sci. Eng., A (2019).

[52] C. Cao, Di Zhang, X. Wang, Q. Ma, L. Zhuang, J. Zhang, Effects of Cu addition on the precipitation hardening response and intergranular corrosion of Al-5.2Mg-2.0Zn (wt.%) alloy, Mater. Charact. 122 (2016) 177–182.

[53] T. Masuda, Y. Takaki, T. Sakurai, S. Hirosawa, Combined effect of pre-straining and pre-aging on bake-hardening behavior of an Al-0.6 mass%Mg-1.0 mass%Si alloy, Mater. Trans. 51 (2010) 325–332.

[54] L. Ding, Z. Jia, Y. Liu, Y. Weng, Q. Liu, The influence of Cu addition and pre-straining on the natural aging and bake hardening response of Al-Mg-Si alloys, J. Alloys Compd. 688 (2016) 362–367.

[55] X.-M. Wang, W.-Z. Shao, J.-T. Jiang, G.-A. Li, X.-Y. Wang, L. Zhen, Quantitative analysis of the influences of pre-treatments on the microstructure evolution and mechanical properties during artificial ageing of an Al–Cu–Li–Mg–Ag alloy, Mater. Sci. Eng., A 782 (2020) 139253.

[56] F. Schmid, L. Stemper, S. Pogatscher, T. Ebner, Industry-oriented sample preparation of 6xxx and 5xxx aluminum alloys in laboratory scale, GDMB (Ed.), EMC 2019: Optimum Utilization Of Resources And Recycling For A Sustainable Solution, 2019.

[57] B. Gruber, I. Weißensteiner, T. Kremmer, F. Grabner, G. Falkinger, A. Schökel, F. Spieckermann, et al., Mechanism of low temperature deformation in aluminium alloys, Mater. Sci. Eng. 795 (2020) 139935.

[58] P. Dumitraschkewitz, P.J. Uggowitzer, S.S.A. Gerstl, J.F. Löffler, S. Pogatscher, Size-dependent diffusion controls natural aging in aluminium alloys, Nat. Commun. 10 (2019) 4746.

[59] M.A. Tunes, C. Quick, L. Stemper, D.S.R. Coradini, J. Grasserbauer, T. Kremmer, P.J. Uggowitzer, et al., A contamination-free electron-transparent metallic sample preparation method for MEMS experiments with in situ S/TEM - submitted 10/2020, Microsc. Microanal. (2020).

[60] M.A. Tunes, L. Stemper, G. Greaves, P.J. Uggowitzer, S. Pogatscher, Prototypic lightweight alloy design for stellar-radiation environments, Adv. Sci. (2020) 2002397.

[61] C.A. Schneider, W.S. Rasband, K.W. Eliceiri, NIH Image to ImageJ: 25 years of image analysis, Nat. Methods 9 (2012) 671–675.

[62] B. Gault, M.P. Moody, F. de Geuser, G. Tsafnat, A. La Fontaine, L.T. Stephenson, D. Haley, et al., Advances in the calibration of atom probe tomographic reconstruction, J. Appl. Phys. 105 (2009) 34913.

[63] P. Felfer, A.V. Ceguerra, S.P. Ringer, J.M. Cairney, Detecting and extracting clusters in atom probe data: a simple, automated method using Voronoi cells, Ultramicroscopy 150 (2015) 30–36.

[64] MATLAPThe MathWorks Inc a, Natick, Massachusetts, 2019 2019.

[65] A. Cerezo, L. Davin, Aspects of the observation of clusters in the 3-dimensional atom probe, Surf. Interface Anal. 39 (2007) 184–188.

[66] A.B. Spierings, K. Dawson, P. Dumitraschkewitz, S. Pogatscher, K. Wegener, Microstructure characterization of SLM-processed Al-Mg-Sc-Zr alloy in the heat treated and HIPed condition, Addit. Manuf. 20 (2018) 173–181.

[67] A.V. Ceguerra, M.P. Moody, L.T. Stephenson, R.K. Marceau, S.P. Ringer, A three-dimensional Markov field approach for the analysis of atomic clustering in atom probe data, Philos. Mag. 90 (2010) 1657–1683.

[68] P. Dumitraschkewitz, S.S.A. Gerstl, P.J. Uggowitzer, J.F. Löffler, S. Pogatscher, Atom probe tomography study of as-quenched Al-Mg-Si alloys, Adv. Eng. Mater. 19 (2017) 1600668.

[69] R.A. Karnesky, C.K. Sudbrack, D.N. Seidman, Best-fit ellipsoids of atom-probe tomographic data to study coalescence of γ' (L12) precipitates in Ni–Al–Cr, Scr. Mater. 57 (2007) 353–356.

[70] P. Giannozzi, S. Baroni, N. Bonini, M. Calandra, R. Car, C. Cavazzoni, D. Ceresoli, et al., Quantum espresso: a modular and open-source software project for quantum simulations of materials, J. Phys. Condens. Matter Inst. Phys. J. 21 (2009) 395502.

[71] Burke Perdew, Ernzerhof, generalized gradient approximation made simple, Phys. Rev. Lett. 77 (1996) 3865–3868.

[72] J.D. Pack, H.J. Monkhorst, Special points for Brillouin-zone integrations, Phys. Rev. B 16 (1977) 1748–1749.

[73] G. Prandini, A. Marrazzo, I.E. Castelli, N. Mounet, N. Marzari, Precision and efficiency in solid-state pseudopotential calculations, NPJ Comput. Mater. 4 (2018).

[74] A. Dal Corso, Pseudopotentials periodic table: from H to Pu, Comput. Mater. Sci. 95 (2014) 337–350.

[75] B. Gruber, F. Grabner, G. Falkinger, A. Schökel, F. Spieckermann, P.J. Uggowitzer, S. Pogatscher, Room temperature recovery of cryogenically deformed aluminium alloys, Mater. Des. 193 (2020) 108819.

[76] H. Mecking, U.F. Kocks, Kinetics of flow and strain-hardening, Acta Metall. 29 (1981) 1865–1875.

[77] G.I. Taylor, The mechanism of plastic deformation of crystals, Proc. R. Soc. Lond. A 145 (1934) 362–387.

[78] C.W. Bale, E. Bélisle, P. Chartrand, S.A. Decterov, G. Eriksson, A.E. Gheribi, K. Hack, et al., FactSage: Thermochemical Software and Databases: Database applied: FTlight, Calphad (2016).

[79] C.B. Carter, D.B. Williams (Eds.), Transmission Electron Microscopy: Diffraction, Imaging, and Spectrometry, Springer International Publishing, Cham, 2016 s.l..

[80] M. von Heimendahl, Electron Microscopy of Materials: An Introduction, Acad. Press, New York, NY, 1980.

[81] J. Zhu, B. Jiang, D. Yi, H. Wang, G. Wu, Precipitate behavior, mechanical properties and corrosion behavior of an Al-Zn-Mg-Cu Alloy during non-isothermal creep aging with axial tension stress, Metals 10 (2020) 378.

[82] S. Maloney, K. Hono, I. Polmear, S. Ringer, The chemistry of precipitates in an aged Al-2.1Zn-1.7Mg at.% alloy, Scr. Mater. 41 (1999) 1031–1038.

[83] F. Cao, J. Zheng, Y. Jiang, B. Chen, Y. Wang, T. Hu, Experimental and DFT characterization of η' nano-phase and its interfaces in Al Zn Mg Cu alloys, Acta Mater. 164 (2019) 207–219.

[84] S.-L. Chen, S. Daniel, F. Zhang, Y.A. Chang, X.-Y. Yan, F.-Y. Xie, R. Schmid-Fetzer et al., *The PANDAT software package and its applications. database: PandatAl2018_TH*, 2002.

[85] S.P. Ringer, K. Hono, T. Skurai, I.J. Polmear, Cluster hardening in an aged Al-Cu-Mg alloy, Scr. Mater. (1997) 517–521.

[86] R. Marceau, G. Sha, R. Ferragut, A. Dupasquier, S.P. Ringer, Solute clustering in Al–Cu–Mg alloys during the early stages of elevated temperature ageing, Acta Mater. 58 (2010) 4923–4939.

[87] R. Ivanov, A. Deschamps, F. de Geuser, Clustering kinetics during natural ageing of Al-Cu based alloys with (Mg, Li) additions, Acta Mater. 157 (2018) 186–195.

[88] M.J. Starink, A model for co-clusters and their strengthening in Al–Cu–Mg based alloys: a comparison with experimental data, IJMR 103 (2012) 942–947.

[89] T. Saito, C.D. Marioara, J. Røyset, R. Holmestad, Effect of low Cu addition and thermo-mechanical history on precipitation in Al-Mg-Si alloys, MSF 794-796 (2014) 1014–1019.

[90] J.-H. Kim, H. Tezuka, E. Kobayashi, T. Sato, Effects of Cu and Ag addition on nanocluster formation behavior in Al-Mg-Si Alloys, Korean J. Mater. Res. 22 (2012) 329–334.

[91] M.W. Zandbergen, A. Cerezo, G. Smith, Study of precipitation in Al–Mg–Si alloys by atom probe tomography II. Influence of Cu additions, Acta Mater. 101 (2015) 149–158.

[92] A. Deschamps, Y. Bréchet, F. Livet, Influence of copper addition on precipitation kinetics and hardening in Al–Zn–Mg alloy, Mater. Sci. Technol. 15 (2013) 993–1000.

[93] N.Q. Chinh, J. Lendvai, D.H. Ping, K. Hono, The effect of Cu on mechanical and precipitation properties of Al–Zn–Mg alloys, J. Alloys Compd. 378 (2004) 52–60.

[94] P.V. Liddicoat, T. Honma, L.T. Stephenson, S.P. Ringer, Evolution of Nanostructure during the Early Stages of Ageing in Al-Zn-Mg-Cu Alloys, MSF 519-521 (2006) 555–560.

[95] S. Medrano, H. Zhao, F. de Geuser, B. Gault, L.T. Stephenson, A. Deschamps, D. Ponge, et al., Cluster hardening in Al-3Mg triggered by small Cu additions, Acta Mater. 161 (2018) 12–20.

[96] Y. Du, Y.A. Chang, B. Huang, W. Gong, Z. Jin, H. Xu, Z. Yuan, et al., Diffusion coefficients of some solutes in fcc and liquid Al: critical evaluation and correlation, Mater. Sci. Eng., A 363 (2003) 140–151.

[97] M.X. Guo, Y.D. Zhang, G.J. Li, S.B. Jin, G. Sha, J.S. Zhang, L.Z. Zhuang, et al., Solute clustering in Al-Mg-Si-Cu-(Zn) alloys during aging, J. Alloys Compd. 774 (2019) 347–363.

[98] J.H. Hollomon, D. Turnbull, Nucleation, Prog. Metal Phys. 4 (1953) 333–388.

[99] A. Deschamps, M. Niewczas, F. Bley, Y. Brechet, J.D. Embury, L.L. Sinq, F. Livet, et al., Low-temperature dynamic precipitation in a supersaturated Al-Zn-Mg alloy and related strain hardening, Philos. Mag. A 79 (1999) 2485–2504.

[100] B. Gruber, F. Grabner, W. Fragner, A. Schökel, F. Spieckermann, P.J. Uggowitzer, S. Pogatscher, Ageing behaviour of Al-Mg-Si alloys after cryogenic and room temperature deformation, Materials (2020) 13.

[101] L.M. Cheng, W.J. Poole, J.D. Embury, D.J. Lloyd, The influence of precipitation on the work-hardening behavior of the aluminum alloys AA6111 and AA7030, Metall. Mater. Trans. A 34 (2003) 2473–2481.

[102] A.R. Massih, Diffusion-controlled phase growth on dislocations†, Philos. Mag. 89 (2009) 3075–3086.

[103] M. Legros, G. Dehm, E. Arzt, T.J. Balk, Observation of giant diffusivity along dislocation cores, Science 319 (2008) 1646–1649.

[104] J.D. Robson, Deformation Enhanced diffusion in aluminium alloys, Metall. Mater. Trans. A 51 (2020) 5401–5413.

[105] S.E. Donnelly, Some solved and unsolved problems in transmission electron microscopy studies of radiation damage in solids, in: P. Sigmund (Ed.), Ion Beam Science: Solved and Unsolved Problems, Det Kongelige Danske Videnskabernes Selskab, Copenhagen, 2006.